This is the peer-reviewed, final accepted version for American Mineralogist, published by the Mineralogical Society of America.
The published version is subject to change. Cite as Authors (Year) Title. American Mineralogist, in press.
DOI: https://doi.org/10.2138/am-2022-8370. http://www.minsocam.org/

Revision 1

Word count: 6887

Stability of Fe_5O_6 and its relation to other Fe-Mg-oxides at high pressures and temperatures

Alan B. Woodland[1]

(Woodland@em.uni-frankfurt.de)

Laura Uenver-Thiele[1]

(Uenver-Thiele@em.uni-frankfurt.de)

Tiziana Boffa Ballaran[2]

(Tiziana.Boffa-Ballaran@Uni-Bayreuth.de)

Nobuyoshi Miyajima[2]

(Nobuyoshi.Miyajima@uni-bayreuth.de)

Kevin Rosbach[1]

(rosbach@stud.uni-frankfurt.de)

Takayuki Ishii[2,3]

(takayuki.ishii@hpstar.ac.cn)

[1]Institut für Geowissenschaften, Goethe-Universität Frankfurt, Altenhöferallee 1, D – 60438 Frankfurt am Main, Germany

[2]Bayerisches Geoinstitut, Universität Bayreuth, D – 95440 Bayreuth, Germany

[3] Now at Center for High Pressure Science and Technology Advanced Research, Beijing, 100094, China

Abstract

The stability of Fe_5O_6 has been experimentally determined under pressure-temperature conditions relevant for the Earth's deeper upper mantle down to the

upper portion of the lower mantle (to 28 GPa). In addition, we investigated the incorporation of Mg into Fe_5O_6 and its systematics, which allows us to discuss the relevance of this phase for the mantle. Experiments were performed from 8-28 GPa and 900-1600°C. Additional oxide phases may appear if the bulk composition does not maintain the $Fe^{2+}_3Fe^{3+}_2O_6$ stoichiometry during the experiment, including coexisting Fe_4O_5 or Fe_9O_{11}. Unfortunately, the similarities in Raman spectra between a number of high-pressure Fe-oxide phases make this method unsuitable for distinguishing which phase is present in a given sample. The stability field for Fe_5O_6 extends from ~9 to at least 28 GPa, but is truncated at lower temperatures by the assemblage Fe_4O_5 + wüstite. Refined thermodynamic properties for Fe_5O_6 are presented. The range of redox stability of Fe_5O_6 appears to be more limited than that of Fe_4O_5.

Solid solution along the Fe_5O_6-$Mg_3Fe_2O_6$ binary is quite limited, reaching a maximum Mg content of ~0.82 cations per formula unit (i.e. $X_{Mg3Fe2O6} \approx 0.27$) at 1400°C and 10 GPa. The observed sharp decrease in molar volume of the O_6-phase with Mg content could be a possible explanation for the limited range of solid solution. A phase diagram has been constructed for a composition of approximately $Mg_{0.5}Fe^{2+}_{2.5}Fe^{3+}_2O_6$ stoichiometry. This small amount of Mg causes a significant change in the relations between the O_6-structured phase and the assemblage O_5-structured phase + (Mg,Fe)O. Several experiments were performed to test whether the O_6-phase can coexist with mantle silicates like wadsleyite and ringwoodite. In all cases, the run products contained $(Mg,Fe)_2Fe_2O_5$ rather than the O_6-phase, further underlining the limited ability of Fe_5O_6 to accommodate enough Mg to be stable in a mantle assemblage.

The large stability field of Fe_5O_6 implies that this phase could likely occur in locally Fe-rich environments, like those sampled by some "deep" diamonds. However, the limited solubility of Mg in the O_6-phase leads us to conclude that the O_5-phase should be of much more relevance as an accessory phase in a peridotitic mantle assemblage.

Key words: Fe-oxide, Fe-Mg-oxide, Fe_5O_6, Fe_4O_5, high pressure, high temperature, phase stability, inclusion in diamond, wüstite, magnetite

Introduction

The recent high-pressure synthesis of a number of new mixed-valence Fe-oxide phases with different stoichiometries indicates that phase relations in the Fe–O system at conditions corresponding to the deeper mantle can be quite complicated. Along with the well-known minerals hematite, magnetite and wüstite, the orthorhombic-structured phases $Fe^{2+}_2Fe^{3+}_2O_5$ and $Fe^{2+}_3Fe^{3+}_2O_6$ (Lavina et al. 2011; Woodland et al. 2012; Woodland et al. 2015; Lavina and Meng, 2015) and the monoclinic-structured phases $Fe^{2+}_3Fe^{3+}_4O_9$ and $Fe^{2+}_5Fe^{3+}_4O_{11}$ (Sinmyo et al. 2016; Ishii et al. 2018) have been synthesised at pressures in excess of ~10 GPa. All four of these oxides lie compositionally between wüstite and magnetite, with each phase having its own $Fe^{3+}/\sum Fe$. Of course the $Fe^{3+}/\sum Fe$ of each phase can be modified through the formation of solid solutions with other cations like Mg, Cr and Al (e.g. Uenver-Thiele et al. 2018).

The relevance of these Fe-oxides for the mineralogy of the Earth's interior rests upon the extent of their stability in terms of pressure, temperature and oxidation state. Nearly pure magnetite has been reported as a rare inclusion in diamond (e.g. Stachel et al. 1998; Jacob et al. 2016), but a precursor phase may have originally formed at depth rather than magnetite

itself (Uenver-Thiele et al. 2017b). Currently, very little information is available on the phase relations involving these four Fe-oxides. The maximum pressure stability of magnetite and its breakdown to Fe_4O_5 + hematite was described by Woodland et al. (2012). Myhill et al. (2016) reported on the minimum pressure stability of Fe_4O_5 and provided a thermodynamic framework for estimating the stabilities of Fe_4O_5 and Fe_5O_6. A recent in situ diamond-anvil study by Hikosaka et al. (2019) indicates that both Fe_4O_5 and Fe_5O_6 remain stable up to nearly 40 GPa, but the actual extent of their respective phase fields and their relative redox relations remain poorly constrained.

We have undertaken an experimental study focussed on the stability of Fe_5O_6 under pressure-temperature conditions relevant for the Earth's deeper upper mantle down to the upper portion of the lower mantle. Our results allow us to better constrain the thermodynamic properties for this phase compared to the initial estimates provided by Myhill et al. (2016, 2018). We go on to describe the incorporation of Mg into Fe_5O_6 and discuss the conditions necessary for this phase to be present in the Earth's mantle.

Experimental and analytical methods

Several different starting materials were employed for the high-pressure experiments. For Fe_5O_6, Fe_6O_7 and Fe_9O_{11} bulk compositions, stoichiometric mixtures of metallic Fe and pre-synthesized magnetite were used. The magnetite was produced by reducing Fe_2O_3 in a gas-mixing furnace at 1300°C and 1 bar in a 1:99 mixture of $CO:CO_2$, yielding an oxygen fugacity of $\log fO_2$= -5.5, which corresponds to the condition where magnetite is stoichiometric (Dieckmann, 1982). The resulting magnetite had a unit-cell parameter of a_o = 8.3966(6) Å. For the Mg-bearing experiments, a mixture of magnetite, Fe metal and either high-purity (99.99%) MgO or a pre-synthesized spinel with composition $MgFe_2O_4$ was employed as starting materials. Several experiments were conducted with a mixture of pre-synthesized forsterite (Mg_2SiO_4) and a $(Mg_{0.5},Fe_{2.5})Fe_2O_6$ stoichiometry comprised of magnesioferrite,

magnetite and Fe metal to verify the stability of oxide phases in a silicate-bearing assemblage.

The starting materials were packed into Ag-, Au- or Pt-foil capsules, depending on starting material and whether the experimental conditions were above the melting point of Ag. All but four experiments with Mg-free compositions employed Ag as capsule material (Table 1). Most Mg-bearing experiments employed Pt capsules since the relatively high oxygen fugacities (fO_2) imposed by the high Fe^{3+}/Fe^{2+} in the starting materials act to minimize any Fe-loss to the Pt. Several repeat experiments using Ag foil yielded the same results as the initial experiments employing Pt foil.

The high-pressure and high-temperature experiments were carried out at the Goethe-Universität Frankfurt and the Bayerisches Geoinstitut, Bayreuth. A 800 t Walker type multi-anvil press was employed in Frankfurt with an experimental setup and pressure calibration as described by Brey et al. (2008). For several experiments performed at 18 GPa, the pressure was calibrated using the wadsleyite to ringwoodite transformation in Mg_2SiO_4 (1200°C, 18 GPa; Inoue et al. 2006). Tungsten carbide anvils with truncated edge lengths of 4 mm or 8 mm were used along with 10 mm- or 14 mm-edged Cr_2O_3-doped MgO octahedra, respectively (the smaller being used for the 18 GPa experiments).

At the Bayerisches Geoinstitut three multi-anvil presses were employed up to 23 GPa: HYMAG MA-6/8 1000 t split-sphere-type press, Zwick 5000 t press and a Voggenreiter Walker-type press. These presses have been cross-calibrated over a wide range in temperature (at least 800-1800°C, see Keppler and Frost 2005). In addition, two experiments were performed at 28 GPa using a 1500 t Kawai-type multi-anvil press with the Osugi-type guide block system, IRIS-15 (Ishii et al. 2016; 2019).

The high-pressure assembly in Frankfurt includes a Re-foil furnace, whereas a $LaCrO_3$ heater is employed in Bayreuth. A W_5/Re_{95}–W_{26}/Re_{74} thermocouple with the electromotive force uncorrected for pressure was used to monitor the temperature. After compression, a heating rate of ~50 °C/min was used. The experiments were terminated by turning off the power and followed by decompression. Uncertainties in pressure and

temperature are ± 0.5 GPa and ± 30-50 °C, respectively (Keppler and Frost 2005). For the experiments at 28 GPa, uncertainties are ± 0.5 GPa and ± 50°C (Liu et al. 2017).

The run products were analyzed by electron microprobe (EPMA) and X-ray powder diffraction. Microprobe analyses were carried out with a five-spectrometer JEOL JXA-8900 Superprobe or a JEOL JXA-8530F plus Hyperprobe using pure MgO Fe_2O_3 and $CaSiO_3$ as primary standards. The EPMA was operated in wavelength-dispersive mode with an acceleration voltage of 15 kV, probe current of 20 nA and a spot size of 1 µm. Integration time for Fe and Mg was 40 sec on the peak while an integration time of 20 sec and 40 sec on the background was set for Fe and Mg, respectively. For Si, counting times of 30 sec on the peak and 15 sec on background were chosen. To verify phase homogeneity, up to four spot analyses were performed on a single grain. A CITZAF algorithm was employed for matrix correction (Armstrong 1993). Backscattered electron (BSE) images were used to study the sample texture.

Raman spectra were obtained on a number of samples using a Witec confocal micro-Raman spectrometer (Alpha300R) equipped with a 532nm Nd:YAG laser and a diffraction grating with 1800 grooves mm^{-1} at the Goethe Universität Frankfurt. Spectrometer calibration was performed with a Hg-Ar lamp. Unpolarized Raman spectra were collected over five accumulations with a 50x microscope objective and a laser power of ~2-3 mW. These conditions were chosen to minimize laser-induced oxidation of the sample, which otherwise was observed to produce hematite during the measurement. The wavenumber accuracy is ± 1-2 cm^{-1} and the focused laser spot on the sample was approximately ~2 µm in diameter.

Powder X-ray diffraction patterns were obtained using a STOE Stadi P diffractometer operating at 45 kV and 35 mA and using monochromatic Mo Kα (λ = 0.70926 Å) radiation, equipped with a linear PSD or a Mythen detector at the Goethe-Universität Frankfurt. The samples were mounted in a 0.5 mm diameter capillary together with a small amount of silicon that served as an internal standard. Diffraction patterns were collected in transmission mode between 1°-100° 2 θ. For a couple of samples, powder diffraction patterns were measured with a Philips X´Pert PRO diffractometer employing monochromatic Co Kα (λ = 1.78897 Å)

radiation selected with a focusing monochromator, a symmetrically cut curved Johansson Ge (111) crystal and a Philips X'celerator detector at the Bayerisches Geoinstitut. These samples were ground together with Si and dispersed on a Si wafer using ethanol. Data were collected between 10° and 120° 2 θ at 40 kV and 40 mA. Preliminary phase identification was routinely carried out using CrystalDiffract software from Crystalmaker Software Ltd. (U.K.). All patterns were analysed with the General Structure Analysis System (GSAS, Larson and van Dreele 1994) software package with the EXPGUI interface of Toby (2001) for phase identification and to determine unit-cell parameters.

Transmission electron microscopic (TEM) investigations were carried out with a Philips CM20FEG TEM, operated at 200 kV, at the Bayerisches Geoinstitut. Dark field TEM images with target diffraction spots and selected area electron diffraction (SAED) patterns of Fe_4O_5, Fe_5O_6 and the hp-$MgFe_2O_4$ phase were obtained from powdered fragments deposited on Lacey carbon-coated copper grids and conventional Ar-milled thin-foils after separation from petrographic thin sections.

Stability and phase relations of Fe_5O_6

Synthesised crystals of Fe_5O_6 are jet black with a metallic luster (Fig. 1) and not visibly different from Fe_4O_5. Unfortunately, Raman spectroscopy is unsuitable for distinguishing between Fe_5O_6, Fe_4O_5 and Fe_9O_{11} since spectra from these three phases are all very similar with one large peak at ~660 cm^{-1} and two subsidiary peaks at ~300 cm^{-1} and 530 cm^{-1} (Fig. 2). The only differences between the phases are slight shifts in the positions of the three peaks. These spectra are also similar to that of magnetite, whose peaks are shifted to higher wave numbers by ~10 cm^{-1} (Fig. 2). It must also be noted that the Fe-oxide phases are all susceptible to oxidiation to hematite during a Raman measurement, necessitating the use of low laser energies. This situation leaves powder X-ray diffraction as the primary method for identifying the phase or phases present in the experimental run products. The experimental conditions and duration, along with the resulting run products are summarised

194 in Table 1. It is clear that the stability field of Fe_5O_6 is quite large, beginning near 9.0 GPa
195 and extending to at least 28 GPa (Fig. 3). At 8 GPa, the assemblage magnetite + wüstite is
196 stable. Two experiments at 9.0 GPa (M651, M785) produced the three-phase assemblage
197 wüstite + Fe_3O_4 + Fe_5O_6, which along with several other experiments (Table 1) allows us to
198 constrain the position of the equilibrium:
199
200 Fe_3O_4 + 2 wüstite = Fe_5O_6 (1)
201
202 to be described by
203
204 P (GPa) = 1.86 x 10^{-3} T (K) + 6.107
205
206 This boundary has only a small temperature dependence, with a slight positive slope (Fig. 3).
207 It essentially coincides with the low-pressure boundary for Fe_4O_5 reported by Myhill et al.
208 (2016), indicating that it is the instability of magnetite that is driving reaction (1) and the
209 analogous reaction involving Fe_4O_5; which high-pressure phase appears depends on the
210 bulk $Fe^{3+}/\sum Fe$ of the starting material. At higher pressures and relatively low temperatures,
211 the stability of Fe_5O_6 is limited by the equilibrium:
212
213 Fe_5O_6 = Fe_4O_5 + wüstite (2)
214
215 Together with an experiment at 14 GPa and 900°C (M736) that yielded all three phases and
216 several bracketing experiments at higher pressures up to 28 GPa (Fig. 3), the position of
217 equilibrium (2) can be approximated by
218
219 P (GPa) = 27.7 x 10^{-3} T (K) - 18.48
220

A phase field for Fe_4O_5 + wüstite instead of Fe_5O_6 at relatively low temperatures was also reported by Hikosaka et al. (2019), confirming the existence of equilibrium (2). However, we find a significantly larger stability field for Fe_5O_6 than their study indicates (Fig. 3). This discrepancy is no doubt related to the large uncertainties in their in situ temperature and pressure determinations, particularly at low temperatures when using laser-heating.

The positions of equilibria (1) and (2) in P-T space are not consistent with the thermodynamic data of Myhill et al. (2016, 2018) for high-pressure Fe-oxide phases as they yield negative P-T slopes, when they should both be positive. This most likely lies with the limited constraints that Myhill et al. had at the time for the properties of Fe_5O_6. Using our new phase diagram (Fig. 3), we can now improve on the Fe_5O_6 properties. Together with data for magnetite taken from Holland & Powell (2011) and for "FeO" and Fe_4O_5 from Myhill et al. (2016, 2018), we begin by adopting the heat capacity function of Myhill et al. (2016, 2018) for Fe_5O_6, which is based on the summation of heat capacities of magnetite and two times that for stoichiometric "FeO" from Holland and Powell (2011) (i.e. Fe_3O_4 + 2FeO). The room temperature equation of state was likewise taken from Myhill et al. (2016, 2018), including the bulk modulus reported by Lavina & Meng (2015). We then refined the standard H°, S° and thermal expansion coefficient for Fe_5O_6 by simultaneously considering constraints from the positions of both equilibria (1) and (2). The non-stoichiometry of coexisting wüstite (Table 1) was accounted for with the model presented by Myhill et al. (2016) and using the compositions from our experiments derived from the relationship between cell parameter and composition given by McCammon and Liu (1984). Our refined thermodynamic properties for Fe_5O_6 are given in Table 2. The new thermal expansion coefficient for Fe_5O_6 is now closer to that of Fe_4O_5 (Myhill et al. 2018), which is consistent with the similarities in their respective crystal structures.

Stability of related Fe-oxides with Fe_5O_6

Even when Fe_5O_6 is stable, an additional phase may appear in the experiments when the bulk composition did not have exactly a $Fe^{2+}{}_3Fe^{3+}{}_2O_6$ stoichiometry. This can be understood by considering a simple chemographic diagram for the FeO–$FeO_{1.5}$ binary system (Fig. 4). In several cases, starting materials with a Fe_6O_7 or Fe_9O_{11} bulk composition were deliberately employed to investigate the phase relations in more detail and test whether additional phase stoichiometries could be stable (Table 1). However, the same effect may occur to a lesser degree due to the difficulty in producing a completely homogeneous starting material involving rather small amounts of metallic Fe powder mixed together with magnetite. In addition, there is the potential for small degrees of oxidation or reduction occurring during the experiment, which can shift the bulk composition of the sample off of its nominal stoichiometry (Woodland et al. 2013). When an excess of Fe^{2+} is present, wüstite appears as an additional phase together with Fe_5O_6 (Table 1). This means that under the pressure-temperature conditions explored so far, no additional phase with a composition lying between wüstite and Fe_5O_6, such as Fe_6O_7, was found to be stable (Fig. 4).

When the sample has a slight excess of Fe^{3+}, Fe_5O_6 usually coexists with Fe_4O_5. However, in a number of experiments Fe_9O_{11} was present (Table 1). This latter phase has a monoclinic structure (Ishii et al. 2018) and a composition intermediate between Fe_5O_6 and Fe_4O_5 (Fig. 4). Based upon its occurrence in our experiments, the stability of Fe_9O_{11} appears to be limited to pressures of 9-14 GPa (Fig. 3), which is much more restricted than observed for either Fe_5O_6 or Fe_4O_5 (Table 1; Myhill et al. 2016). In one experiment, both Fe_4O_5 and Fe_9O_{11} occurred together with Fe_5O_6 (M733, Table 1). This is probably due to a small variation in Fe^{3+}/Fe^{2+} across the sample, which was subsequently homogenised for the powder diffraction measurement. However, in two other cases (at 10 and 12 GPa, respectively) Fe_4O_5 rather than Fe_9O_{11} appeared to coexist with Fe_5O_6 (Table 1). Although this might suggest that Fe_9O_{11} is metastable, its large abundance in several other experiments, along with being well crystallised as judged by the sharp reflections in the X-ray diffraction diagrams argues against this interpretation. In addition, this phase has also been synthesised in Mg-bearing compositions (Ishii et al. 2018 and see below).

This is the peer-reviewed, final accepted version for American Mineralogist, published by the Mineralogical Society of America.
The published version is subject to change. Cite as Authors (Year) Title. American Mineralogist, in press.
DOI: https://doi.org/10.2138/am-2022-8370. http://www.minsocam.org/

The coexistence of Fe_5O_6 and Fe_4O_5 at least at P ≥ 14 GPa defines a redox equilibrium according to

$$5\ Fe_4O_5 = 4\ Fe_5O_6 + 0.5\ O_2 \quad (3)$$

Combining thermodynamic data for Fe_5O_6 from Table 2, along with data for Fe_4O_5 and O_2 from Myhill et al. (2018) and Stagno & Frost (2010), respectively, we can compute the oxygen fugacity of this equilibrium as a function of pressure and temperature. The result is illustrated in Figure 5 as a function of pressure at 1200°C, along with several other oxygen buffer equilibria for reference. The upper redox limit for Fe_4O_5 is defined by its equilibrium with hematite (i.e. $2\ Fe_2O_3 = Fe_4O_5 + 0.5\ O_2$), indicating that this phase has a redox stability that extends over 4-5 log units in fO_2. In the process of calculating the fO_2 of equilibria involving wüstite, it became evident that the solid solution model of Myhill et al. (2016, 2018) is not consistent with the wüstite compositions observed in our experiments. As a result, we are currently unable to map out the P-T-fO_2 relations of wüsitite-bearing equiliria with either Fe_5O_6 or Fe_4O_5. Nevertheless, from Figure 5 it is apparent that the redox stability of Fe_5O_6 must be much more limited than that of Fe_4O_5 particularly at higher pressures since the redox stability fields for both Fe_5O_6 and wüstite must lie between equilibrium (3) and the Fe-wüstite buffer (Holland & Powell 2011) and there is only a difference of 3-4 log units in fO_2 between these equilibria.

For a Fe_3O_4 bulk composition, Woodland et al. (2012) observed the high-pressure assemblage of Fe_4O_5 + hematite to extensively back react to magnetite. However, the more reduced bulk compositions of this study (i.e. Fe_4O_5, Fe_5O_6, Fe_9O_{11}, Fe_6O_7) allowed the high-pressure oxide phase(s) to be recovered. This suggests that it is the reactivity of Fe_4O_5 in the presence of hematite that drives the back reaction. Even when the high-pressure oxide phases are recovered, care needs to be taken during sample characterisation. For example, although no deleterius effects were observed during microprobe analysis, the higher energy electron beam and small volume of analysis during TEM investigation can cause local

reversion to magnetite during a measurement if precautions are not taken. Thermal cycling even at low temperatures < 300 K during measurements of magnetic properties can also induce magnetite formation (C. Krellner, pers. comm.). Anecdotal evidence suggests that Fe_4O_5 may be more inclined to reversion to magnetite ± wüstite during and after the quench compared to Fe_5O_6 or Fe_9O_{11}. For example, the run products from experiments at ≥18 GPa that produced the assemblage Fe_4O_5 + wüstite contained variable amounts of secondary magnetite that had an anomalously large cell parameter $a_o \approx 8.42$ Å (Table 1). Although more detailed analysis is still warranted, we consider this indicative of a defect spinel structure, where a normally unoccupied crystallographic site is occupied by Fe^{2+}, allowing its composition to approach that of the initial Fe_4O_5 stoichiometry. TEM investigation of sample Z1585u revealed very extensive {113} polysynthetic twinning in magnetite (Fig. 6) and such twinning has been reported to occur by back reaction from Fe_4O_5 (Schollenbruch et al. 2011; Myhill et al. 2016). Electron diffraction measurements of this magnetite also yielded an abnormally large cell parameter of $a_o \approx 8.42$ Å, consistent with that observed by XRD. That this defect magnetite formed at the expense of Fe_4O_5 can also be demonstrated from two XRD patterns of sample M639 obtained 6 months apart. The relative intensities of diffraction peaks for Fe_4O_5 were markedly higher compared to those of defect magnetite and wüstite in the earlier pattern obtained just after the experiment. Apparently the Fe_4O_5 in the finely ground powdered sample (mixed with Si powder) continued to react to magnetite ± metastable wüstite even at room temperature on the time scale of months.

Incorporation of Mg in Fe_5O_6

A further series of experiments were undertaken to investigate the incorporation of Mg in Fe_5O_6 (Table 3). Experiments with Mg-rich bulk compositions ($Mg_2Fe^{2+}Fe^{3+}{}_2O_6$ or $MgFe^{2+}{}_2Fe^{3+}{}_2O_6$) did not produce a Fe_5O_6-structured phase. Instead, the run products contained either (i) O_5-phase + unquenchable phase or (ii) O_5-phase + (Mg,Fe)O. For example, experiment M760, with a bulk composition $Mg_2Fe^{2+}Fe^{3+}{}_2O_6$, revealed an O_5-solid

This is the peer-reviewed, final accepted version for American Mineralogist, published by the Mineralogical Society of America.
The published version is subject to change. Cite as Authors (Year) Title. American Mineralogist, in press.
DOI: https://doi.org/10.2138/am-2022-8370. http://www.minsocam.org/

solution coexisting with another phase that had broken down at the end of the experiment to a very fine mixture of ferropericlase and a magnesioferrite-rich spinel, as detected by X-ray diffraction. Unfortunately the very fine grain size precluded chemical analysis of the individual phases. However, the bulk composition of this unquenchable phase could be determined from repeated large-diameter microprobe analyses to have a Mg/(Mg+∑Fe) = 0.51 (isopleth indicated in Fig. 7). This composition is consistent with a $(Mg,Fe^{2+})_4Fe^{3+}{}_2O_7$ phase, which would be collinear with the compositions of the starting material and the O_5-phase present (Fig. 7; Table 4). Such an unquenchable phase is consistent with the observations of Uenver-Thiele et al. (2017a), who investigated the high-pressure breakdown of magnesioferrite.

An O_6-structured phase was only obtained in bulk compositions with lower Mg contents where a $(Mg_{0.5}Fe^{2+}{}_{2.5})Fe^{3+}{}_2O_6$ or $(Mg_{0.6},Fe^{2+}{}_{3.4})Fe^{3+}{}_2O_7$ starting composition with Mg# = 0.167 or 0.15 was employed (Table 3). Use of the slightly more reduced O_7 bulk composition was intended to compensate for potential oxidation that might occur during the experiment. Our results demonstrate not only that the $Mg_3Fe_2O_6$ endmember is unstable, but that solid solution along the Fe_5O_6-$Mg_3Fe_2O_6$ binary is quite limited. We obtained a maximum Mg content of ~0.82 cations per formula unit (i.e. $X_{Mg3Fe2O6} \approx 0.27$) at 1400°C and 10 GPa (Table 4). Unlike for the Mg-rich composition just described, there was no textural evidence for an unquenchable phase with O_7 stoichiometry having been present during these experiments. This is also consistent with our observations in the Mg-free system that no further phases are stable with compositions lying between Fe_5O_6 and wüstite.

A series of experiments with a $Mg_{0.5}Fe^{2+}{}_{2.5}Fe^{3+}{}_2O_6$ starting composition allowed us to construct the phase relations at high P and T (Fig. 8). Like for Fe_5O_6, the minimum P stability of the Mg-bearing O_6-phase lies at ≈ 9 GPa. On the other hand, comparison with Figure 3 reveals that the addition of only ~0.5 cations Mg to the bulk composition significantly changes the slope of the phase boundary between the O_6-phase and the assemblage O_5 + magnesiowüstite. This change in slope is likely related to differences in the thermodynamic properties (Mg,Fe)O solid solutions in comparison to wüstite. For example, the unit cell

parameters obtained in this study exhibit strong deviations from those reported by O'Neill et al. (2003), indicating a significant presence of Fe^{3+} in ferropericlase at high pressures (Table 3). Unfortunately, the Fe^{3+} contents could not be quantified by Mössbauer spectroscopy due to the multiphase nature of our run products.

As described for the Mg-free experiments, additional phases may appear in an experiment due to either local heterogeneities in the starting material or from small degrees of oxidation or reduction occuring during the experiment. This is illustrated in Figure 9 where the phase assemblages for experiments at 12 GPa are depicted. In addition, traces of carbonate were detected in some experiments, presumably due to reaction between adsorbed CO_2 and the starting material (Table 3). In several experiments at 12 and 14 GPa, a phase with Fe_9O_{11} stoichiometry appeared that also contained Mg (Table 3, Fig. 9), indicating some oxidation had occurred, increasing the bulk Fe^{3+} content from the stoichometric value for the O_6-phase. The effect of Mg incorporation on the crystal structure of Fe_9O_{11} has been detailed by Ishii et al. (2018). In other experiments at conditions where the O_{11}-phase was not stable, $(Mg,Fe)_2Fe_2O_5$ and/or magnesiowüstite appeared in the assemblage (Table 3).

Coexistence with silicates?

To explicitly test if the O_6-phase could also coexist with mantle silicates, several experiments were performed over a pressure range of 14-20 GPa using a starting bulk compositon of 70 % $Mg_{0.5}Fe_{2.5}Fe_2O_6$ and 30 % forsterite (Tables 3, 4). In all cases, the run products contained $(Mg,Fe)_2Fe_2O_5$ coexisting with magnesiowüstite and either wadsleyite or ringwoodite. This is consistent with the results of Sinmyo et al. (2019), who found Mg-bearing Fe_4O_5 coexisting with bridgmanite at 26 GPa and 1400°C. In our experiments, the silicate phase reacted to incorporate a significant Fe-component of 0.35-0.40 mol % Fe_2SiO_4 (Table 4). Wadsleyite or ringwoodite is still the phase richest in Mg in the assemblage and the O_5-phase contains the least Mg. This agrees with the results described by Uenver-Thiele et al.

(2018) for experiments with higher bulk Fe^{3+} contents. The Mg-Fe partitioning systematics between ringwoodite and the coexisting magnesiowüstite yield a K_D = 0.22-0.24 ($X_{Mg}^{Si} X_{Fe}^{mw}$/ $X_{Fe}^{Si} X_{Mg}^{mw}$), which agrees with earlier experiments performed under oxidising conditions (Ito & Takahashi 1989; Frost et al. 2001) and suggests that Mg-Fe exchange in our experiments had reached equilibrium. The Mg-bearing Fe_4O_5 was also found to incorporate only very small amounts of Si, consistent with that found by Woodland et al. (2013) for Mg-free compositions. We observe a slight increase in Si content with increasing pressure from 0.16 wt % to 0.33 wt % SiO_2 going from 14 to 20 GPa (Table 4), which corresponds to 0.008 and 0.15 cations per formula unit. This is much less than reported by Sinmyo et al. (2019), who found up to 1.6-2.4 wt % SiO_2 in their Mg-bearing Fe_4O_5 coexisting with bridgmanite and stishovite at 26 GPa. However, we note that our experiments did not contain stishovite and thus had a lower silica activity.

These three experiments further document the relative instability of the Fe_5O_6 crystal structure compared to Fe_4O_5 in Mg-bearing bulk compositions. Apparently the Mg-Fe^{2+} partitioning with a Mg-rich wadsleyite or ringwoodite would require the O_6-phase to have a Mg content that exceeds its stability range (e.g. see Uenver-Thiele et al. 2018).

Structural systematics of $(Fe,Mg)_3Fe^{3+}{}_2O_6$

The Fe_5O_6 endmeber. In spite of repeated attempts, the crystal quality of samples of Fe_5O_6 proved insufficient for a full single-crystal structural analysis. This was due either to internal stress in the crystals, the occurrence of subgrain boundaries, or the partial back transformation to a defect magnetite structure. In any case, the qualitative results from single-crystal X-ray diffraction at least confirm that Fe_5O_6 belongs to the *Cmcm* space group, making it a member of the $CaFe_{2+n}O_{4+n}$ series (with n=2; Evrard et al. 1980), like Fe_4O_5. At ambient conditions, the cell paramters are *a* = 2.88 Å, *b* = 9.94 Å, *c* = 15.37 Å, with small variations between samples (Table 5). In some cases, differences in cell parameters can be attributed to the influence of peak overlap with coexisting phases in the diffraction pattern. No

obvious correlations between the measured molar volume or individual cell parameters and synthesis conditions are observable (Table 5). This is also the case for samples coexisting with either Fe_4O_5 or wüstite, suggesting that this Fe_5O_6 is essentially stoichiometric. We obtain an average room temperature molar volume of 66.35(4) cm^3 (n=18) for the Fe_5O_6 endmember, which agrees perfectly with the earlier values reported by Lavina and Meng (2015) and Woodland et al. (2015).

Mg-bearing compositions. As described previously, solid solution along the Fe_5O_6-$Mg_3Fe_2O_6$ binary is very limited to a maximum of $X_{Mg3Fe2O6} \approx 0.27$. Compared with Fe_5O_6, incorporation of Mg causes the greatest change in shortening the *b*-cell parameter. As expected, the molar volume of the recovered $(MgFe^{2+})_3Fe^{3+}{}_2O_6$ solid solutions decreases systematically with increasing Mg content (Table 4; Fig. 10). It is notable that the relative change in molar volume on a per Mg-cation basis is significantly greater than for analogous $(Mg,Fe^{2+})_2Fe^{3+}{}_2O_5$ solid solutions (compare Fig. 10 with Fig. 8 in Uenver-Thiele et al. 2018). Although not conclusive, this sharp reduction in molar volume could provide an explanation for why the O_6-structure becomes destabilised with the addition of Mg.

Implications of Fe_5O_6 for the Earth's mantle

The stability field for Fe_5O_6 defined in this study suggests that it could be an accesory phase from the deep upper mantle (~300 km), through the transition zone and into the lower mantle at least down to ~925 km (Fig.1). In fact, Hikosaka et al. (2019) indicate that both Fe_5O_6 and Fe_4O_5 remain stable up to ~38 GPa (> 1200 km depth) where they both become destabilized by the appearance of orthorhombic-structured hp-Fe_3O_4. This stability range makes both phases candidates for becoming incorporated as inclusions in diamond. On the one hand, considering the rather reduced redox conditions expected in the mantle, assemblages involving Fe_5O_6 should have the most relevance for the Earth, following the suggestion of Myhill et al. (2016). On the other hand, the position of equilibrium (3) reveals that Fe_4O_5 has

a redox stability that extends over 4-5 log units in fO_2 and stradles the transition where diamond and carbonate (magnesite) are stable in a peridotitic bulk composition. Thus, if diamond were to form through coupled reduction of carbonate and oxidation of Fe (e.g. Palyanov et al. 2002), then Fe_4O_5 would potentially be the more likely phase to be trapped during diamond growth.

In the process of transporting materials containing Fe_5O_6 or Fe_4O_5 to the surface, it is very likely that the high-pressure phase will not be preserved, even if it is encapsulated in a diamond. In fact, back-reaction to magnetite is often observed on the short time scale of quenching and decompressing an experiment in the laboratory (this study, Schollenbruch et al. 2011; Woodland et al. 2012; Myhill et al. 2016). Aside from texural evidence, several features may be used to interpret whether a given phase was stable at the conditions of the experiment or whether a precursor phase was originally present. For example, polysynthetic twins parallel to {113} have been reported in magnetite that formed by back reaction from Fe_4O_5 (Schollenbruch et al. 2011; Myhill et al. 2016). In this study, we have observed the same twinning in magnetite that had transformed from Fe_5O_6 in sample M758 (Fig. 6). Considering the similarity in the crystal structures of Fe_4O_5 and Fe_5O_6, it is perhaps not surprising {113}-parallel twinning can form in magnetite during transformation from either of these phases at low pressures. Thus, the twinned magnetite corona observed by Jacob et al. (2016) growing on a pyrrhotite inclusion in a diamond from the Orapa Mine could have had either Fe_4O_5 or Fe_5O_6 as a high-pressure precursor. Further features indicative of a high-pressure precursor phase to magnetite are the presence of antiphase domains and mottling in dark field TEM images (Fig. 11a, 11b). Although antiphase domains have not been reported in natural magnetite up to now, this may be more due to such structures not being looked for in the past. Considering the potential for subsequent annealing of such structures, they are more likely to be preserved in shocked meteorites than in samples from the deep Earth, the later potentially remaining at high temperatures for long periods of time.

As a number of studies have identified nearly pure magnetite as an inclusion in diamond (e.g. Stachel et al. 1998; Jacob et al. 2016), it is clear that local environments

anomalously Fe-rich must exist in the deep mantle, at least where diamond forms. But the 'normal' mantle assemblage is dominated by Mg-rich bulk compositions. However, our study indicates that the extent of Mg-incorporation in Fe_5O_6 is quite limited. In fact, our experiments with Si-bearing bulk compositions produced assemblages with the O_5-phase rather than the O_6-phase. Even in these experiments, ringwoodite and wadsleyite had $X_{Mg} \approx 0.60$-0.65, which is still significantly richer in Fe than expected for a peridotitic bulk composition (i.e. $X_{Mg} \approx 0.9$). Thus, we conclude that in the peridotitic mantle assemblage the O_5-phase should be of much more relevance as an accessory phase than the O_6-phase.

Acknowledgements

This study was supported by the Deutsche Forschungsgemeinschaft through grants Wo 652/20-2 and BO 2550/7-2 to A.B.W. and T.B.B., respectively. E. Alig was very helpful in obtaining the X-ray powder diffraction pattern and C. Heckel aided with the microprobe measurements. We are grateful to Thomas Kautz and Svyatoslav Shcheka for their help with the multi-anvil experiments in Frankfurt and Bayreuth. Fruitful discussions with Dan Frost and Gerhard Brey are gratefully acknowledged. The comments of two anonymous reviewers improved the manuscript.

References

Brey, G.P., Bulatov, V., and Girnis, A. (2008) Geobarometry for peridotites: experiments in simple and natural systems from 6 to 10 GPa. Journal of Petrology, 49, 3–24.

Dieckmann R. (1982) Defects and Cation Diffusion in Magnetite (IV): Nonstoichiometry and Point Defect Structure of Magnetite ($Fe_{3-\delta}O_4$). Bericht der Bunsenges. Journal of Physical Chemistry, 86, 112-118.

Evrard, O., Malaman, B., Jeannot, F., Courtois, A., Alebouyeh, H., and Gerardin, R. (1980). Mise en évidence de $CaFe_4O_6$ et détermination des structures cristallines des ferrites de

calcium $CaFe_{2+n}O_{4+n}$ (n=1, 2, 3): nouvel exemple d'intercroissance. Journal of Solid State Chemistry, 35, 112-119.

Frost, D.J., Langenhorst, F., and van Aken, P.A. (2001) Mg–Fe partitioning between ringwoodite and magnesiowüstite and the effect of pressure temperature and oxygen fugacity. Physics and Chemistry of Minerals, 28, 455-470.

Hikosaka, K., Sinmyo, R., Hirose, K., Ishii, T., and Ohishi, Y. (2019) The stability of Fe_5O_6 and Fe_4O_5 at high pressure and temperature. American Mineralogist, 104, 1356-1359.

Holland, T.J.B., and Powell, R. (2011) An improved and extended internally consistent thermodynamic dataset for phases of petrological interest, involving a new equation of state for solids. Journal of Metamorphic Geology, 29, 333–383.

Inoue, T., Irfune, T., Higo, Y., Sanehira, T., Sueda, Y., Yamada, A., Shinmei, T., Yamazaki, D., Ando, J., Funakoshi, K., and Utsumi, W. (2006) The phase boundary between wadsleyite and ringwoodite in Mg2SiO4 determined by in situ X-ray diffraction. Physics and Chemistry of Minerals, 33, 106–114.

Ishii, T., Liu, Z., and Katsura, T. (2019). A breakthrough in pressure generation by a Kawai-type multi-anvil apparatus with tungsten carbide anvils. Engineering, 5(3), 434-440.

Ishii, T., Shi, L., Huang, R., Tsujino, N., Druzhbin, D., Myhill, R., Li, Y., Wang, L., Yamamoto, T., Miyajima, N., Kawazoe, T., Nishiyama, N., Higo, Y., Tange, Y., and Katsura, T. (2016). Generation of pressures over 40 GPa using Kawai-type multi-anvil press with tungsten carbide anvils. Review of Scientific Instruments, 87(2), 024501

Ishii, T., Uenver-Thiele, L., Woodland, A., Alig, E., and Boffa Ballaran, T. (2018) Synthesis and crystal structure of Mg-bearing Fe_9O_{11}: New insight in the complexity of Fe-Mg oxides at conditions of the deep upper mantle. American Mineralogist, 103, 1873-1876.

Ito, E., and Takahashi, E. (1989) Postspinel transformations in the system Mg2SiO4–Fe2SiO4 and some geophysical implications. Journal of Geophysical Research, 94, 10637-10646.

526 Jacob, D. E., Piazolo, S., Schreiber, A., and Trimby, P. (2016). Redox-freezing and
527 nucleation of diamond via magnetite formation in the Earth's mantle. Nature
528 Communications, 7, 11891.
529 Keppler, H., and Frost, D.J. (2005) Introduction to minerals under extreme conditions. In R.
530 Miletich, Ed., Mineral Behaviour at Extreme Conditions, 7, 1–30. EMU Notes in
531 Mineralogy.
532 Larson, A.C., and Von Dreele, R.B. (2000) General structure analysis system (GSAS). Los
533 Alamos National Laboratory Report, LAUR, 86–748.
534 Lavina, B., Dera, P., Kim, E., Meng, Y., Downs, R.T., Weck, P.F., Sutton, S.R., and Zhao, Y.
535 (2011) Discovery of the recoverable high-pressure iron oxide Fe_4O_5. Proceedings of the
536 National Academy of Science, 108, 17281-17285.
537 Lavina, B., and Meng, Y. (2015) Unraveling the complexity of iron oxides at high pressure
538 and temperature: Synthesis of Fe_5O_6. Science Advances 1, no.5, e1400260.
539 Liu, Z., Nishi, M., Ishii, T., Fei, H., Miyajima, N., Ballaran, T. B., Ohfuji, H., Sakai, T., Wang,
540 L., Shcheka, S., Arimoto, T., Tange, Y., Higo, Y., Irifune, T., and Katsura, T. (2017)
541 Phase relations in the system $MgSiO_3$-Al_2O_3 up to 2300 K at lower mantle
542 pressures. Journal of Geophysical Research: Solid Earth, 122(10), 7775-7788.
543 McCammon, C.A., and Liu, L. (1984) The effects of pressure and temperature on non-
544 stoichiometric wüstite, FexO: The iron-rich phase boundary. Physics and Chemistry of
545 Minerals, 10, 106-113.
546 Myhill, B., Ojwang, D.O., Ziberna, L., Frost, D., Boffa Ballaran, T., and Miyajima, N. (2016)
547 On the P-T-fO_2 stability of Fe_4O_5 and Fe_5O_6-rich phases: a thermodynamic and
548 experimental study. Contributions to Mineralogy and Petrology, 171, 1-11.
549 Myhill, B., Ojwang, D.O., Ziberna, L., Frost, D., Boffa Ballaran, T., and Miyajima, N. (2018)
550 Correction to: On the P-T-fO_2 stability of Fe_4O_5 and Fe_5O_6-rich phases: a thermodynamic
551 and experimental study. Contributions to Mineralogy and Petrology, 173, 3.

O'Neill, H.St.C., Pownceby, M.I., and McCammon, C.A. (2003) The magnesiowüstite: iron equilibrium and its implications for the activity-composition relations of $(Mg,Fe)_2SiO_4$ olivine solid solutions. Contributions to Mineralogy and Petrology, 146, 308-325.

Palyanov, Y.U., Sokol, A.G., Borzdov, Y.M., and Khokhryakov, A.F. (2002) Fluid-bearing alkaline carbonate melts as the medium for the formation of diamonds in the earth's mantle: an experimental study. Lithos, 60, 145-159.

Schollenbruch, K., Woodland, A.B., Frost, D.J., Wang, Y., Sanehira, T., and Langenhorst, F. (2011) In situ determination of the spinel – post-spinel transition in Fe_3O_4 at high temperature and pressure by synchrotron X-ray diffraction. American Mineralogist, 96, 820-827, DOI: 10.2138/am.2011.3642

Sinmyo, R., Bykova, E., Ovsyannikov, S.V., McCammon, C., Kupenko, I., Ismailova, L., and Dubrovinsky, L. (2016) Discovery of Fe_7O_9: a new iron oxide with a complex monoclinic structure. Nature Scientific Reports, 6, 32852.

Sinmyo, R., Nakajima, Y., McCammon, C.A., Miyajima, N., Petitgirard, S., Myhill, R., Dubrovinsky, L., and Frost, D.J. (2019). Effect of Fe^{3+} on phase relations in the lower mantle: Implications for redox melting in stagnant slabs. Journal of Geophysical Research: Solid Earth, 124, 12484-12497.

Stachel, T., Harris, J.W., and Brey, G.P. (1998) Rare and unusual mineral inclusions in diamonds from Mwadui, Tanzania. Contributions to Mineralogy and Petrology, 132, 34–47.

Stagno, V., and Frost, D.J. (2010) carbon speciation in the asthenosphere: Experimental measurements of the redox conditions at which carbonate-bearing melts coexist with graphite or diamond in peridotite assemblages. Earth and Planetary Science Letters, 300, 72-84.

Toby, B.H. (2001) EXPGUI, a graphical user interface for GSAS. Journal of Applied Crystallography, 34, 210-213.

578 Uenver-Thiele L, Woodland AB, Boffa Ballaran T, Miyajima N, and Frost DJ (2017a) Phase
579 relations of $MgFe_2O_4$ at conditions of the deep upper mantle and transition zone.
580 American Mineralogist, 102, 632-642.
581 Uenver-Thiele, L., Woodland, A.B., Boffa Ballaran, T., Miyajima, N., and Frost, D.J. (2017b)
582 Phase relations of Fe-Mg spinels including new high-pressure post-spinel phases and
583 implications for natural samples. American Mineralogist, 102, 2054-2064.
584 Uenver-Thiele, L., Woodland, A.B., Miyajima, N., Boffa Ballaran, T., and Frost, D.J. (2018)
585 Behavior of Fe_4O_5−$Mg_2Fe_2O_5$ solid solutions and their relation to coexisting Mg-Fe
586 silicates and oxide phases. Contributions to Mineralogy and Petrology, 173, 20
587 Woodland, A.B., Frost, D.J., Trots, D.M., Klimm, K., and Mezouar, M. (2012) In situ
588 observation of the breakdown of magnetite (Fe_3O_4) to Fe_4O_5 and hematite at high
589 pressures and temperatures. American Mineralogist, 97, 1808-1811.
590 Woodland, A.B., Schollenbruch, K., Koch, M., Boffa Ballaran, T., Angel, R.J., and Frost, D.J.
591 (2013) Fe_4O_5 and its solid solutions in several simple systems. Contributions to
592 Mineralogy and Petrology, 166, 1677-1686. (DOI) 10.1007/s00410-013-0948-4.
593 Woodland, A. B., Uenver-Thiele, L., and Boffa Ballaran, T. (2015) Synthesis of Fe_5O_6 and the
594 High-Pressure Stability of Fe^{2+}-Fe^{3+}-oxides related to Fe_4O_5. Goldschmidt Abstracts
595 2015, 3446.

596

597 Tables

598

599 Table 1 Conditions and run products of experiments in the Fe–O system along with refined
600 cell parameters of magnetite and wüstite and derived wüstite composition
601 Table 2 Revised thermodynamic properties of the Fe_5O_6 endmember composition
602 Table 3 Summary of experiments in the system MgO–FeO–$FeO_{1.5}$ ± SiO_2 along with the
603 composition and volume of coexisting (Mg,Fe)O
604 Table 4 Composition, unit cell parameters and volumes of run products from experiments in
605 the system MgO–FeO–$FeO_{1.5}$ ± SiO_2

606 Table 5 Cell parameters of Fe_5O_6, Fe_4O_5 and Fe_9O_{11}

607

608 Figure captions

609

610 Fig. 1 Photomicrograph of Fe_5O_6 crystals.

611

612 Fig 2. Raman spectra of the high-pressure Fe-oxides and magnetite. The small peaks
613 marked by * are from a trace of hematite produced during the measurement.

614

615 Fig 3. Phase diagram for Fe_5O_6. The points marked with "O5" indicate that Fe_5O_6 coexists
616 with Fe_4O_5 in these experiments, just like the square symbols indicating the coexistence
617 of Fe_9O_{11} with Fe_5O_6. This coexistence indicates small deviations from the ideal sample
618 stoichiometry (see text). The diamond marked by "L&M" denotes the synthesis
619 conditions of Fe_5O_6 reported by Lavina and Meng (2015). The dashed line is the phase
620 boundary for equilibrium (2) (Fe_5O_6 = Fe_4O_5 + wüstite) reported by Hikosaka et al.
621 (2019) with the stability field for Fe_5O_6 lying on the higher temperature side of the
622 boundary.

623

624 Fig. 4 Chemographic diagram for the binary system FeO-$FeO_{1.5}$ illustrating different phases
625 found to be stable at different pressures and temperatures.

626

627 Fig. 5 Plot of fO_2 versus pressure at 1200°C for several equilibria involving Fe_4O_5 and Fe_5O_6.
628 Several other redox buffers are also shown for reference, calculated using data from
629 Myhill et al. (2016, 208) for Fe_5O_6 and from Holland & Powell (2011): IW = iron-wüstite;
630 EMOD = enstatite-magnesite-olivine-diamond; EMWD = enstatite-magnesite-wadsleyite-
631 diamond; EMRD = enstatite-magnesite-ringwoodite-diamond. The EMOD, EMWD and
632 EMRD curves merge into each other where the phase transitions occur in Mg_2SiO_4.

633

Fig. 6 Dark field TEM image and the corresponding selected area electron diffraction pattern of sample Z1585u revealing extensive polysynthetic twinning parallel to the (131) plane in magnetite that had back reacted from Fe_5O_6.

Fig. 7 Chemographic analysis of the run products in sample M760 with a bulk composition $Mg_2Fe^{2+}Fe^{3+}{}_2O_6$ (star). The orange cross indicates the composition of the coexisting O_5-phase, as determined by EPMA. The isopleth at $Mg/(Mg+Fe_{tot}) = 0.51$ represents the composition of the unquenchable phase originally present at the pressure and temperature of the experiment, as obtained from microprobe analyses employing a large beam diameter to obtain an "average" composition. The yellow cross represents the interpreted composition of the unquenchable $(Mg,Fe^{2+})_4Fe^{3+}{}_2O_7$ phase.

Fig. 8. P-T phase diagram for the $(Mg_{0.5},Fe_{2.5})Fe_2O_6$ bulk composition

Fig. 9. Diagram of the MgO-FeO-$FeO_{1.5}$ system illustrating phase relations in four experiments performed at 12 GPa. Small and variable degrees of oxidation or reduction are indicated by arrows.The star denotes the starting composition.

Fig. 10. Variation in cell parameters of $(Mg,Fe)_3Fe_2O_6$ solid solutions as a function of the mole fraction of $Mg_3Fe_2O_6$.

Fig. 11. Dark field TEM images of a) antiphase domains in magnetite that formed by backreaction from Mg-bearing Fe_5O_6 in sample M697. RS = rock salt structure (i.e. wüstite) and b) mottled contrast in iron oxide back-transformed from Fe_5O_6 in sample V888 (view with *g* = 311). The lower left and upper right insets are SAED patterns of the nearest zone axis and the corresponding diffraction pattern to the dark field image, respectively, which indicate the presence of back-reacted magnetite.

This is the peer-reviewed, final accepted version for American Mineralogist, published by the Mineralogical Society of America.
The published version is subject to change. Cite as Authors (Year) Title. American Mineralogist, in press.
DOI: https://doi.org/10.2138/am-2022-8370. http://www.minsocam.org/

Table 1. Conditions and run products of experiments in the Fe–O system along with refined cell parameters of r

experiment	starting stoichiometry	pressure [GPa]	temperature [°C]	duration [hr]	run products[1]	cell parameter wüstite [Å]	FexO[2]
H4346	Fe_5O_6	8	1000	4.5	mt+wü	4.2825(1)	0.892
H4348o[4]	Fe_5O_6	8	1350	1	mt+wü	4.2912(1)	0.91
M786	Fe_6O_7	9	800	5.5	Fe_5O_6+Fe_9O_{11}+wü	4.2768(1)	0.88
M774	Fe_9O_{11}	9	1000	4	Fe_4O_5+(Fe_9O_{11})		
M651	Fe_6O_7	9	1200	4.5	Fe_5O_6+wü+mt	4.2842(1)	0.896
M785	Fe_6O_7	9	1310	3	Fe_5O_6+wü+mt	4.2844(1)	0.896
M777[5]	Fe_9O_{11}	9	1350	2.5	Fe_4O_5+mt+(wü)+(Fe_9O_1	4.2969(6)	0.922
M756[5]	Fe_9O_{11}	9	1500	1	mt+wü+(Fe_4O_5)	4.2888(3)	0.905
M728	Fe_5O_6	10	900	5	Fe_5O_6		
M653	Fe_6O_7	10	1000	6	Fe_5O_6		
V838	Fe_4O_5	10	1100	4	Fe_4O_5+Fe_5O_6		
V888	Fe_5O_6	10	1200	4.5	Fe_5O_6 (+wü)		
M587	Fe_5O_6	10	1200	3.75	Fe_5O_6 (+wü)		
Z1505[4]	Fe_5O_6	11	1500	2.67	Fe_5O_6+Fe_9O_{11}		
V889	Fe_5O_6	12	1200	4	Fe_5O_6+Fe_4O_5		
V891	Fe_6O_7	12	1200	2.67	Fe_5O_6+wü	4.2980(2)	0.925
M614	Fe_5O_6	12	1200	3	Fe_5O_6+Fe_9O_{11}		
M733	Fe_5O_6	13	1000	4	Fe_5O_6+Fe_4O_5		
M736	Fe_5O_6	14	900	4.5	Fe_5O_6+Fe_4O_5+wü	4.3032(2)	0.936
M755	Fe_9O_{11}	14	1500	1	Fe_9O_{11}+Fe_4O_5		
H4269	Fe_5O_6	15	1200	3.5	Fe_5O_6+Fe_4O_5		
H4270	Fe_6O_7	16	1400	3.25	Fe_5O_6+wü	4.2810(1)	0.889
M639	Fe_5O_6	18	1000	4	Fe_4O_5+wü+dmt	4.3019(5)	0.933
M652	Fe_5O_6	18	1000	6	Fe_4O_5+wü+dmt	4.3055(4)	0.94
H4853	Fe_5O_6	18	1100	4.25	Fe_5O_6+(Fe_4O_5)		
Z1430u	Fe_5O_6	18	1300	2.5	Fe_5O_6		
Z1585u	Fe_5O_6	20	1100	3.5	wü+dmt+Fe_4O_5	4.3147(1)	0.96
H4855	Fe_6O_7	20	1150	3	Fe_5O_6+Fe_4O_5		
Z1464u	Fe_5O_6	20	1300	0.67	Fe_5O_6+Fe_4O_5		
Z1507	Fe_6O_7	20	1600	2	Fe_5O_6		

H4347	Fe_5O_6	23	1300	3.67	Fe_5O_6+Fe_4O_5		
IRIS 697	Fe_5O_6	28	1200	3	Fe_4O_5+wü+dmt	4.3188(3)	0.968
IRIS 702	Fe_5O_6	28	1500	1	Fe_5O_6+?		

[1] wü = wüstite, mt = magnetite, dmt = defect-bearing magnetite.
[2] calculated following formulation of McCammon and Liu (1984).
[3] mole fraction of FeO in FeO-$FeO_{1.5}$ solid solution following approach of Myhill et al. (2016).
[4] employed Au capsule
[5] employed Pt capsule

nagnetite and wüstite and derived wüstite composition

$XFeO^3$	cell parameter magnetite [Å]
0.683	8.3966(1)
0.73	8.3945(1)
0.647	
0.695	8.4011(6)
0.694	8.3988(3)
0.77	8.3934(3)
0.72	8.3942(1)
0.779	
0.811	
0.674	
0.803	8.4209(5)
0.82	8.4255(13)
0.88	8.4172(7)

0.906 8.421(2)

This is the peer-reviewed, final accepted version for American Mineralogist, published by the Mineralogical Society of America.
The published version is subject to change. Cite as Authors (Year) Title. American Mineralogist, in press.
DOI: https://doi.org/10.2138/am-2022-8370. http://www.minsocam.org/

Table 2 Thermodynamic data for Fe_5O_6. Heat capacity terms have the form: $a+bT+cT^{-2}+dT^{-0.5}$.

	Fe_5O_6	source
$H°_{1bar,298}$ (kJ mol^{-1})	-1920.3	this study
$S°_{298}$ (J K^{-1} mol^{-1})	279.93	this study
$V°_{298}$ (cm^3 mol^{-1})	66.33	this study
K_o (GPa)	173	Lavina & Meng (2015)
K'	4	Myhill et al. (2018))
K'' (GPa^{-1})	-2.312 e-2	Myhill te al. (2018)
a_o (K^{-1})	2.02 e-5	this study
Cp (J K^{-1} mol^{-1}) a	351.3	Holland & Powell (2011)
b	9.355 e-3	from molar sum of terms
c	-4.3546 e6	for "FeO" and
d	-1.2853 e3	magnetite

This is the peer-reviewed, final accepted version for American Mineralogist, published by the Mineralogical Society of America.
The published version is subject to change. Cite as Authors (Year) Title. American Mineralogist, in press.
DOI: https://doi.org/10.2138/am-2022-8370. http://www.minsocam.org/

Table 3. Summary of experiments in the system MgO–FeO–$FeO_{1.5}$ ± SiO_2 along with the co

experiment	P [GPa]	T [C°]	duration [h]	phase assemblage[1]	(Mg,Fe)O nMg	nFe
$(Mg_2Fe)Fe_2O_4$						
M686	12	1300	1	O_5 + [sp + (Mg,Fe)O]		
M760	12	1500	1	O_5 + [sp + (Mg,Fe)O]		
$(Mg_1Fe_2)Fe_2O_6$						
M764	12	1300	3	O_5 + (Mg,Fe)O + (mgs)	0.31(1)	0.69(1)
M833	14	1300	1	O_5 + (Mg,Fe)O	0.29(1)	0.71(1)
$(Mg_{0.5}Fe_{2.5})Fe_2O_6$						
M719	8	1100	4	O_4 + (Mg,Fe)O		
M737	8	1200	3	O_4 + (Mg,Fe)O + (mgs)	0.121(3)	0.879(3)
M749[2]	8	~1200-1300	1	O_4 + (Mg,Fe)O		
M723	10	1000	5	O_5 + (Mg,Fe)O + (mgs)	0.24(1)	0.76(1)
M729[2]	10	1000	5	O_5 + (Mg,Fe)O	0.207(3)	0.793(3)
M718	10	1200	3	O_5 + (Fe,Mg)O	0.20(1)	0.80(1)
M758	10	1400	1	O_5 + O_6 + MgO		
M706	12	1000	5	O_5 + (Fe,Mg)O	0.23(1)	0.77(1)
M725	12	1200	3	O_5 +(Mg,Fe)O	0.244(2)	0.756(2)
M697	12	1300	3	O_6 + (Mg,Fe)O	0.143(1)	0.857(1)
M702	12	1300	4	O_{11}		
M724	14	1000	5	O_5+(Mg,Fe)O	0.286(8)	0.714(8)
M705	14	1300	3	O_5 + O_6 + ((Fe,Mg)O)	0.18(2)	0.82(2)
M754	14	1500	1	O_6 + (O_{11}) +((Fe,Mg)O)		
M738	14	1600	2	O_{11} + (O_5)		
Z1804o	16	~1130	2	O_5 + O_6+ ((Mg,Fe)O)	0.23(1)	0.77(1)
Z1806u	20	1300	3	O_5 + O_6 + (Mg,Fe)O	0.284(2)	0.716(2)
$(Mg_{0.6}Fe_{3.4})Fe_2O_7$						
M836	10	1100	1	O_5 + (Mg,Fe)O	0.13(1)	0.87(1)
M837	10	1200	1	O_5 + (Mg,Fe)O + (mgs)	0.12(1)	0.88(1)
M834	10	1500	0.67	O_6 + (MgFe)O + sp	0.13(1)	0.87(1)
M835	12	1200	1	O_6 + (MgFe)O + (O_5) + (mg	0.15(1)	0.85(1)

M838	14	1100	1.5	O_6 + (MgFe)O + (mgs)	0.16(1)	0.84(1)
M839	18	900	3	O_5 + (Mg,Fe)O + [sp]		
0.3 Mg_2SiO_4 + 0.7 $(Mg_{0.5}Fe_{2.5})Fe_2O_6$						
M761	14	1300	3	O_5 + wads + (Mg,Fe)O	0.198(2)	0.802(1)
Z1954o	17	1300	1.5	O_5 + ring + (Mg,Fe)O	0.264(1)	0.736(1)
Z1955o	20	1300	1.5	O_5 + ring + (Mg,Fe)O	0.31(1)	069(1)

[1] sp = spinel, mgs = magnesite, wads = wadsleyite, ring = ringwoodite,
square brackets indicate quench phases, curved brackets indicate occurence in trace amounts.
[2] Experiment carried out with silver capsule.

mposition and volume of coexisting (Mg,Fe)O

a_o [Å]	Mol Vol [cm^{-3}]
4.2309(1)	75.735(7)
4.2304(2)	75.706(8)
4.2481(1)	11.542(1)
4.2472(1)	11.534(1)
4.2678(1)	11.703(1)
4.2692(1)	11.714(1)
4.2701(2)	11.722(1)
4.2565(4)	11.610(3)
4.2665(1)	11.692(1)
4.2538(3)	11.588(2)
4.2522(1)	11.575(1)
4.2722(2)	11.739(1)
4.2504(5)	11.560(4)
4.2653(1)	11.682(1)
4.2786(4)	11.792(3)
4.2510(3)	11.565(1)
4.2836(2)	11.847(1)
4.2668(1)	11.695(1)
4.2652(1)	11.682(1)
4.2637(1)	11.670(1)
4.2639(1)	11.671(1)

4.2674(1)	11.700(1)
4.2937(5)	11.917(4)
4.2485(1)	11.545(1)
4.2606(1)	11.644(1)
4.2706(1)	11.726(1)

This is the peer-reviewed, final accepted version for American Mineralogist, published by the Mineralogical Society of America.
The published version is subject to change. Cite as Authors (Year) Title. American Mineralogist, in press.
DOI: https://doi.org/10.2138/am-2022-8370. http://www.minsocam.org/

Table 4. Composition, unit cell parameters and volumes of run products from experiment

experimen	phase	nMg c.p.f.u.	nFe^{2+} c.p.f.u.	nFe3+ c.p.f.u.	unit-cell paramters *a* [Å]	*b* [Å]	*c* [Å]
	$(Mg,Fe)_3Fe_2O_6$						
M834		0.37(1)	2.63(1)	2	2.8904(2)	9.8981(7)	15.3551(9
M838		0.39(2)	2.61(2)	2	2.8905(1)	9.8999(2)	15.3523(3
M835		0.40(2)	2.60(2)	2	2.8905(1)	9.8992(3)	15.3514(4
M697		0.421(6)	2.579(6)	2	2.8909(1)	9.9000(2)	15.3545(3
M754		0.51(1)	2.49(1)	2	2.8923(1)	9.8877(4)	15.3470(5
M705		0.53(2)	2.47(2)	2	2.8925(1)	9.8876(3)	15.3486(4
Z1804o		0.53(4)	2.47(4)	2	2.8977(2)	9.8711(6)	15.3372(8
Z1806u		0.55(2)	2.45(2)	2	2.8855(6)	9.8972(25)	15.3522(2
M758		0.82(1)	2.18(1)	2	2.8925(1)	9.8724(4)	15.3520(6
	$(Mg,Fe)_2Fe_2O_5$						
M837		0.18(1)	1.82(1)	2	2.8923(1)	9.7960(4)	12.5690(4
M836		0.19(1)	1.81(1)	2	2.8926(1)	9.7958(4)	12.5706(4
M724		0.27(2)	1.73(2)	2	2.8937(2)	9.7858(6)	12.5720(7
M729		0.271(4)	1.729(4)	2	2.8925(1)	9.7939(4)	12.5714(4
M706		0.31(5)	1.69(5)	2	2.8920(1)	9.7884(4)	12.5703(5
Z1804o		0.31(4)	1.69(4)	2	2.8930(2)	9.7805(6)	12.5676(6
M723		0.32(3)	1.68(3)	2	2.8937(1)	9.7846(3)	12.5706(3
Z1806u		0.33(1)	1.67(1)	2	2.8923(1)	9.7816(6)	12.5690(6
M725		0.374(4)	1.626(4)	2	2.8932(1)	9.7852(3)	12.5690(4
M718		0.38(2)	1.62(2)	2	2.8927(1)	9.7874(4)	12.5667(4
M839		0.38(2)	1.62(2)	2	2.886(1)	9.777(4)	12.575(4)
M705		0.42(2)	1.58(2)	2	2.8900(5)	9.799(2)	12.563(2)
M758		0.42(1)	1.58(1)	2	2.8921(1)	9.7918(3)	12.5626(4
M764		0.50(1)	1.50(1)	2	2.8934(1)	9.7773(3)	12.5629(3
M833		0.52(1)	1.48(1)	2	2.8930(2)	9.7705(6)	12.5627(6
M686		0.89(2)	1.11(2)	2	2.8922(3)	9.7623(13)	12.5586(1
M760		1.09(1)	0.91(1)	2	2.8922(2)	9.7539(6)	12.5538(6
	$(Mg,Fe)Fe_2O_4$						
M719		0.17(1)	0.83(1)	2	8.3928(1)		
M737		0.171(2)	0.829(2)	2	8.3895(2)		
M760					8.4060(6)		
M749					8.3887(4)		
	$(Mg,Fe)_5Fe_4O_{11}$						
M702		0.867(9)	4.133(9)	4	9.8441(5)	2.8920(1)	14.1760(6
M754		1.46(1)	3.54(1)	4			

This is the peer-reviewed, final accepted version for American Mineralogist, published by the Mineralogical Society of America.
The published version is subject to change. Cite as Authors (Year) Title. American Mineralogist, in press.
DOI: https://doi.org/10.2138/am-2022-8370. http://www.minsocam.org/

M738		1.02(3)	3.98(3)	4	9.8368(2)	2.8927(1)	14.1728(3
Si-bearing samples							
	$(Mg,Fe)_2Fe_2O_5$						
M761		0.32(1)	1.66(1)	1.96(1)[2]	2.8925(2)	9.7792(9)	12.5638(8)
Z1954o		0.38(1)	1.63(1)	1.95(1)[2]	2.8935(1)	9.7662(6)	12.5532(6)
Z1955o		0.36(1)	1.65(1)	1.94(1)[2]	2.8926(4)	9.7683(16)	12.5482(13
	$(Mg,Fe)_2SiO_4$						
M761	wads	1.27(1)	0.68(1)	0.08(1)	5.7349(16)	11.5696(34	8.3153(19)
Z1954o	ring	1.23(1)	0.75(1)	0.04(1)	8.1292(3)		
Z1955o	ring	1.30(2)	0.68(2)	0.03(1)	8.1208(7)		

[1] sp = spinel, mgs = magnesite, wads = wadsleyite, ring = ringwoodite.

[2] contains traces of SiO_2 and Al_2O_3: M761 – 0.16 wt% SiO_2, 0.40 wt % Al_2O_3; Z1954o – 0.21 wt%

Z1955o – 0.33 wt% SiO_2, 0.56 wt% Al_2O_3

This is the peer-reviewed, final accepted version for American Mineralogist, published by the Mineralogical Society of America.
The published version is subject to change. Cite as Authors (Year) Title. American Mineralogist, in press.
DOI: https://doi.org/10.2138/am-2022-8370. http://www.minsocam.org/

ts in the system MgO–FeO–$FeO_{1.5}$ ± SiO_2

β [°]	V [Å^3]	Mol Vol [cm^{-3}]
)	439.30(3)	66.137(4)
)	439.316(10	66.139(2)
)	439.256(14	66.130(2)
)	439.445(9)	66.158(2)
)	438.89(2)	66.075(3)
)	438.959(15	66.085(3)
)	438.70(3)	66.046(4)
9)	438.44(9)	66.007(13)
)	438.39(2)	66.000(3)
)	356.124(14	53.914(3)
)	356.189(15	53.624(3)
)	356.00(2)	53.596(3)
)	356.14(1)	53.617(2)
)	355.847(2)	53.573(1)
)	355.59(2)	53.543(3)
)	355.92(1)	53.584(2)
)	355.59(2)	53.543(3)
)	355.83(1)	53.570(2)
)	355.79(1)	53.654(2)
	354.86(15)	53.42(2)
	355.79(7)	53.564(10)
)	355.760(12	53.560(2)
)	355.406(10	53.506(2)
)	355.10(2)	53.461(3)
1)	354.58(4)	53.382(6)
)	354.14(2)	53.318(3)
	591.17(2)	44.500(2)
	590.48(3)	44.448(3)
	593.96(11)	44.71(1)
	590.32(8)	44.436(7)
99.956(4)	397.50(3)	119.687(9)

	99.906(2)	397.27(1)	119.618(3)
		355.38(3)	53.502(5)
		354.73(2)	53.405(3)
	)	354.55(4)	53.377(6)
		551.7(1)	41.53(1)
		537.21(6)	40.385(8)
		535.5(1)	40.31(1)

; SiO_2, 0.49 wt% Al_2O_3;

Table 5. Unit-cell parameters and volumes of high-P Fe-oxide phases

experiment	phase	*a* [Å]	*b* [Å]	*c* [Å]	*V* [Å^3]	molar Volume [cm^3]
	Fe_5O_6					
H4269		2.8845(1)	9.9442(5)	15.3632(7)	440.68(2)	66.344(3)
H4270		2.8838(1)	9.946384)	15.3642(5)	440.70(2)	66.347(3)
H4347		2.8830(1)	9.9437(5)	15.3600(7)	440.34(2)	66.293(3)
H4853		2.8842(1)	9.9412(3)	15.3643(4)	440.53(1)	66.322(2)
H4855		2.8840(1)	9.9417(3)	15.3634(4)	440.50(1)	66.317(2)
M651		2.8848(4)	9.946(2)	15.361(2)	440.75(8)	66.355(12)
M653		2.8851(1)	9.9475(4)	15.3751(6)	441.26(2)	66.432(3)
M728		2.8834(1)	9.9426(4)	15.3632(5)	440.44(2)	66.308(3)
M733		2.8840(1)	9.9424(5)	15.3646(7)	440.57(2)	66.328(3)
M736		2.8838(3)	9.9414(11)	15.3554(13)	440.23(4)	66.277(6)
M785		2.8880(8)	9.934(3)	15.357(3)	440.56(11)	66.34(2)
M786		2.8848(5)	9.934(2)	15.390(3)	441.04(8)	66.399(12)
V888		2.8855(1)	9.9399(2)	15.3666(2)	440.74(2)	66.353(3)
V889		2.8851(2)	9.9429(6)	15.3678(11)	440.85(3)	66.370(4)
V891		2.8846(1)	9.9448(6)	15.3679(8)	440.90(3)	66.377(4)
Z1430u		2.8842(1)	9.9408(5)	15.3606(6)	440.40(2)	66.302(3)
Z1464u		2.8837(1)	9.9397(5)	15.3602(7)	440.27(2)	66.283(3)
Z1507u		2.8840(1)	9.9457(3)	15.3678(4)	440.81(2)	66.364(3)
	Fe_4O_5					
H4269		2.8917(12)	9.8006(56)	12.5762(51)	356.41(15)	53.66(2)
H4347		2.8938(3)	9.8036(14)	12.5721(14)	356.66(5)	53.695(7)
H4853		2.8930(5)	9.8053(23)	12.5813(24)	356.89(8)	53.730(12)
H4855		2.8926(1)	9.8032(6)	12.5783(7)	356.68(2)	53.698(3)
IRIS 697		2.8939(2)	9.8002(7)	12.5696(7)	356.49(2)	53.670(3)
M639		2.9097(6)	9.7747(27)	12.5558(26)	357.10(9)	53.761(14)
M652		2.8942(3)	9.7975(11)	12.5626(11)	356.23(4)	53.630(6)
M733		2.8936(7)	9.7988(32)	12.5762(30)	356.6(1)	53.69(2)
M736		2.8917(1)	9.8053(4)	12.5777(5)	356.63(2)	53.691(3)
M755		2.8934(2)	9.8046(9)	12.5759(10)	356.76(3)	53.710(5)
M756		2.8908(3)	9.805(3)	12.579(3)	356.5(1)	53.67(2)
M774		2.8914(1)	9.8060(4)	12.5688(4)	356.365(14)	53.651(2)
M777		2.8928(1)	9.8025(4)	12.5778(4)	356.675(13)	53.697(2)
V838		2.8939(1)	9.8054(2)	12.5820(21)	357.028(12)	53.751(2)
V889		2.8959(8)	9.8064(37)	12.5759(48)	357.1(1)	53.76(2)
Z1464u		2.8923(2)	9.8046(8)	12.5710(9)	356.49(3)	53.670(5)
	Fe_9O_{11}					
		a [Å]	*b* [Å]	*c* [Å]	β (°)	*V* [Å^3]
M755		9.8804(2)	2.8857(1)	14.189(7)	99.920(6)	398.50(2)
M774		9.8500(51)	2.8950(15)	14.182(5)	99.95(7)	398.3(2)
M786		9.8666(32)	2.8901(7)	14.185(3)	100.08(3)	398.26(12)
Z1505		9.8841(6)	2.8843(1)	14.1920(7)	99.923(6)	398.54(2)


100µm

Figure 2

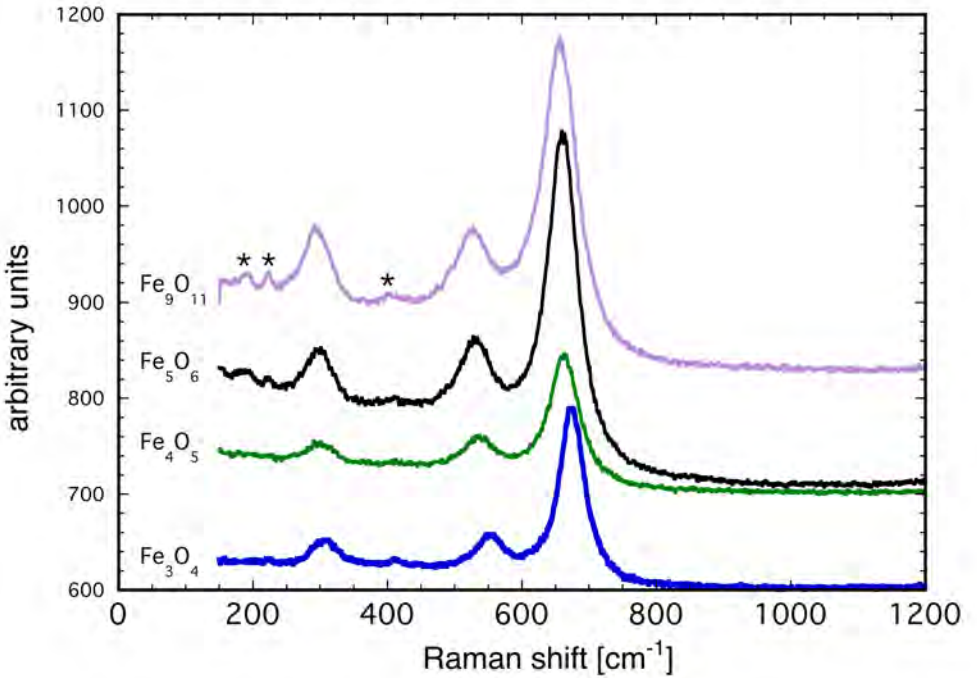
arbitrary units
Raman shift [cm^{-1}]
Fe_9O_{11}
Fe_5O_6
Fe_4O_5
Fe_3O_4
*
*
*
1200
1100
1000
900
800
700
600
0
200
400
600
800
1000
1200

Figure 3

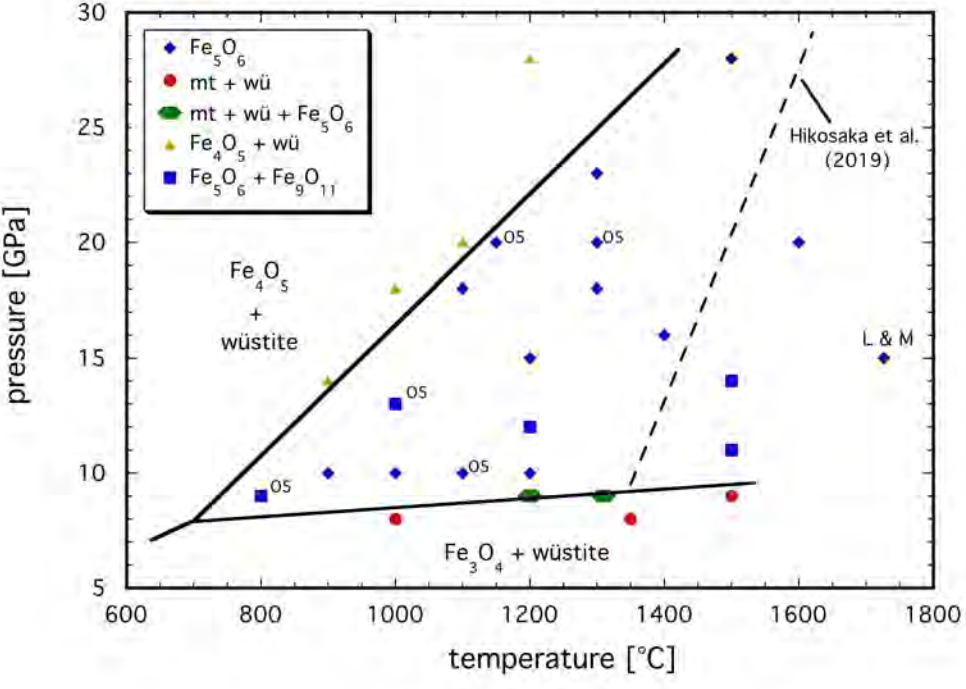
Fe5O6
mt + wü
mt + wü + Fe5O6
Fe4O5 + wü
Fe5O6 + Fe9O11
Fe4O5
+
wüstite
Fe3O4 + wüstite
Hikosaka et al.
(2019)
L & M
O5
pressure [GPa]
temperature [°C]
30
25
20
15
10
5
600
800
1000
1200
1400
1600
1800

Figure 4

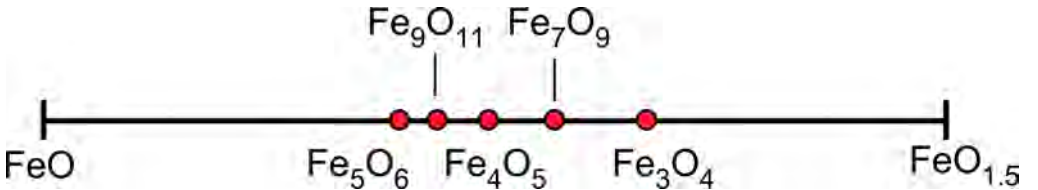

Figure 5

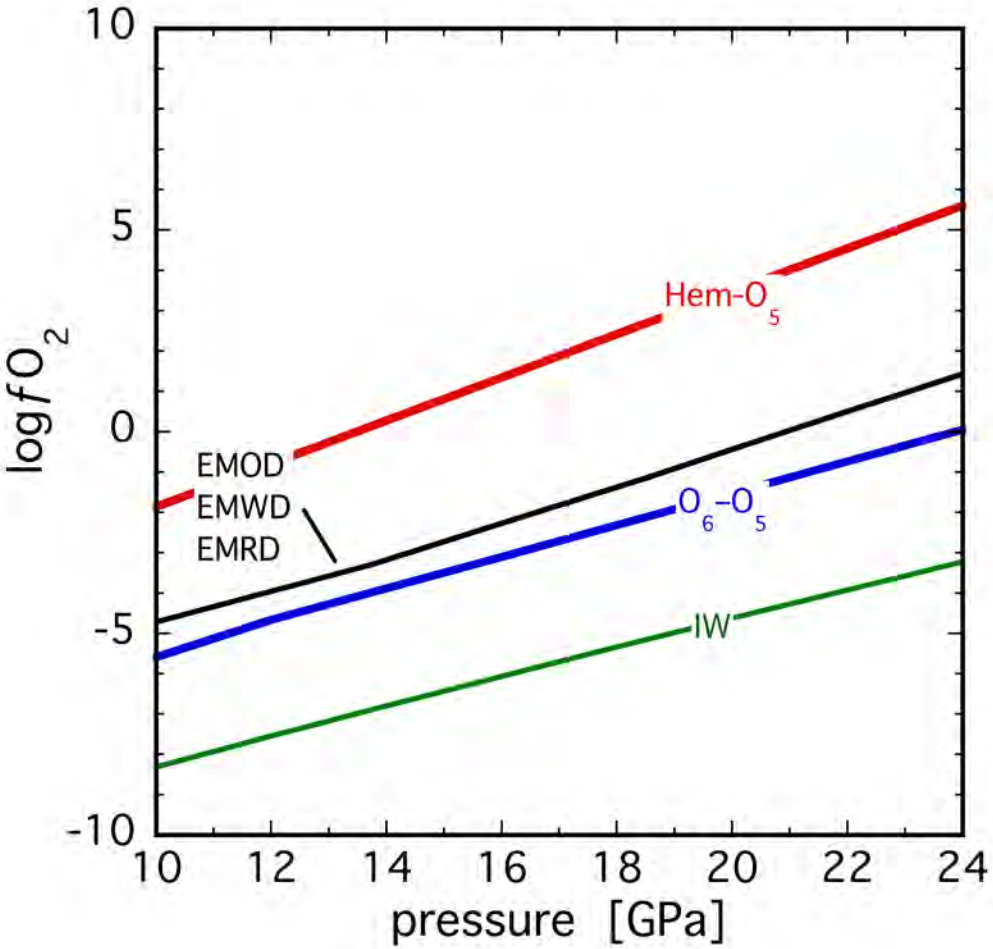
10
5
0
-5
-10
10
12
14
16
18
20
22
24
logfO_2
pressure [GPa]
Hem-O_5
EMOD
EMWD
EMRD
O_6–O_5
IW

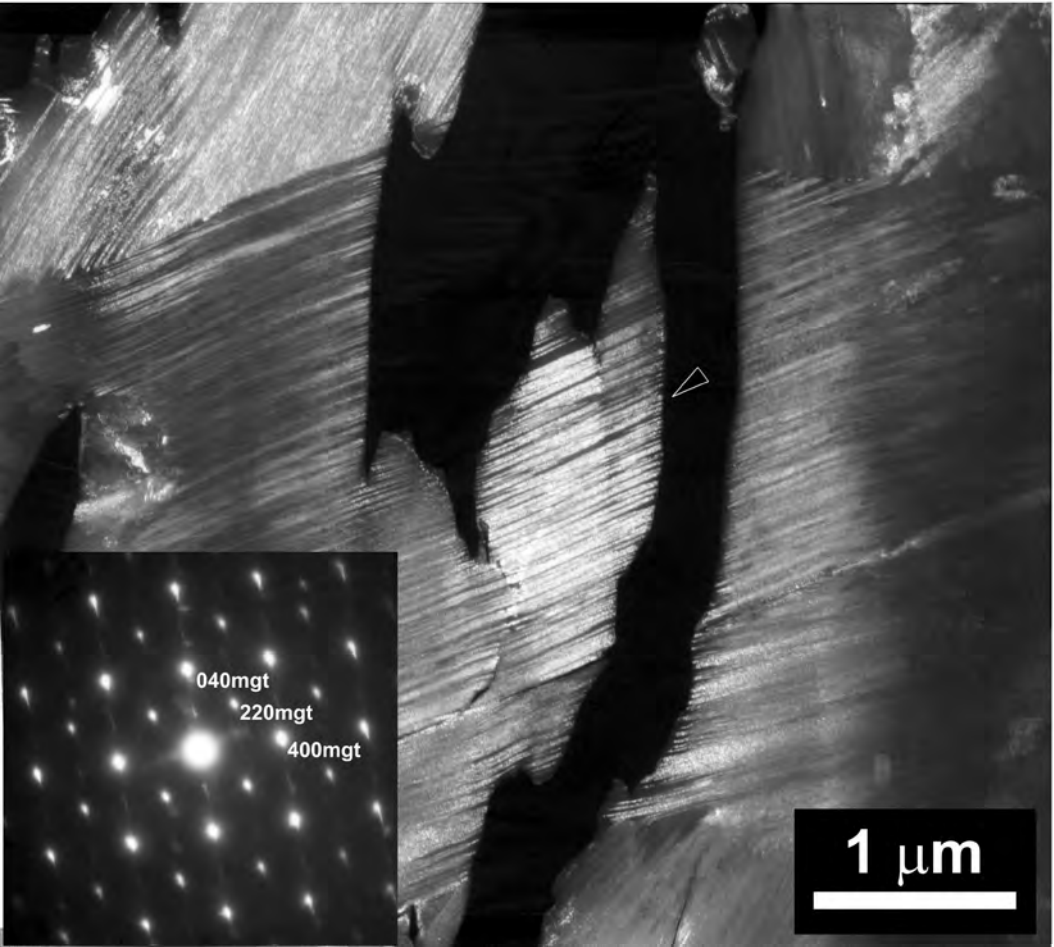
040mgt
220mgt
400mgt
1 μm

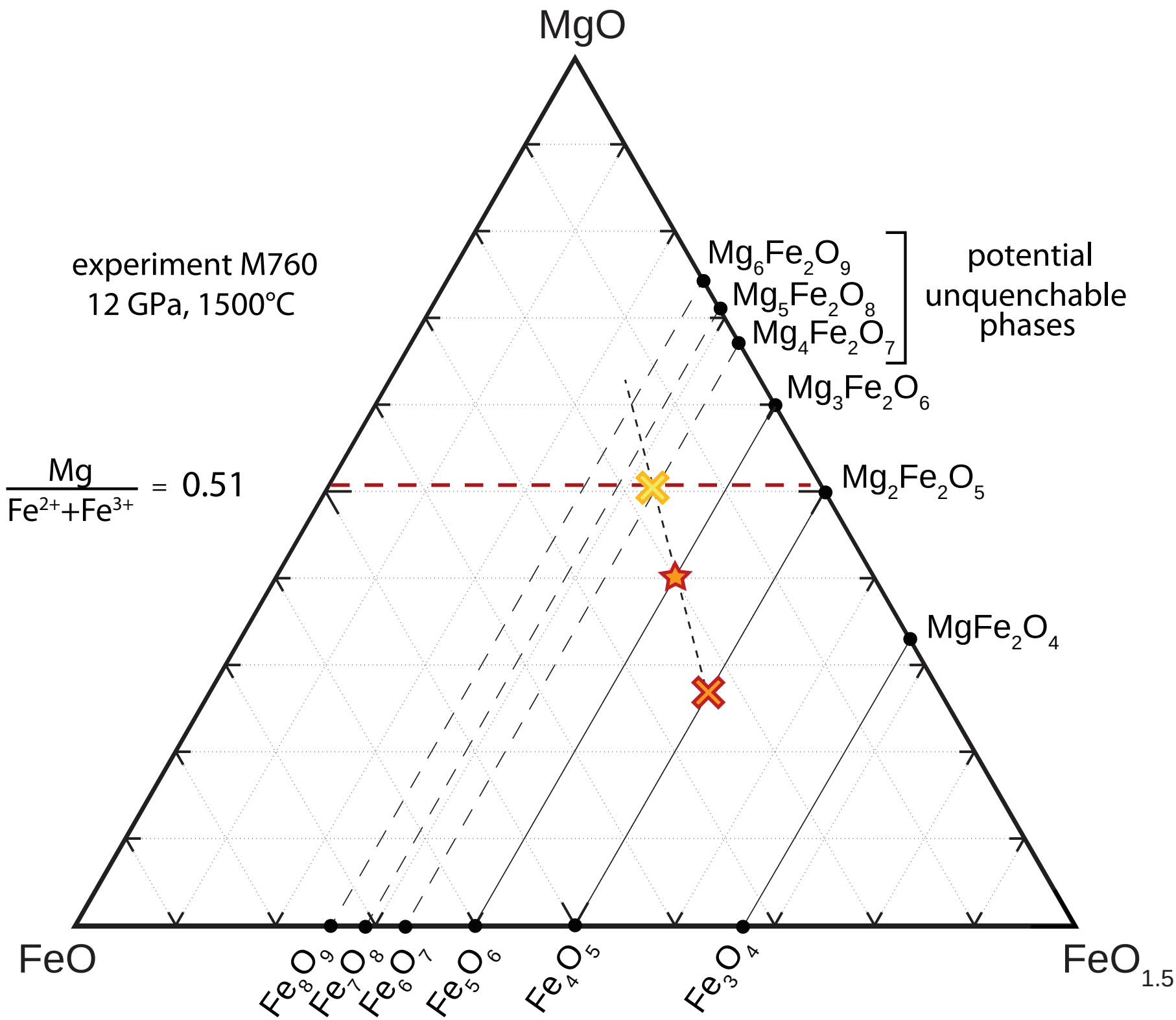
MgO
experiment M760
12 GPa, 1500°C
$\frac{Mg}{Fe^{2+}+Fe^{3+}} = 0.51$
$Mg_6Fe_2O_9$
$Mg_5Fe_2O_8$
$Mg_4Fe_2O_7$
potential unquenchable phases
$Mg_3Fe_2O_6$
$Mg_2Fe_2O_5$
$MgFe_2O_4$
FeO
Fe_8O_9
Fe_7O_8
Fe_6O_7
Fe_5O_6
Fe_4O_5
Fe_3O_4
$FeO_{1.5}$

Figure 8

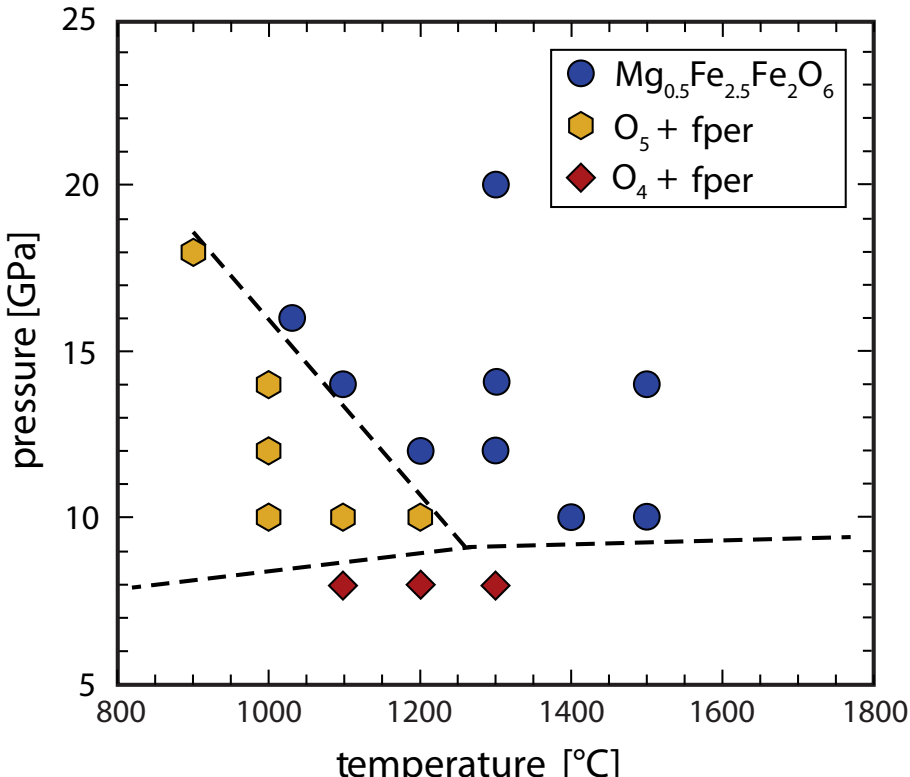
25
20
15
10
5
800
1000
1200
1400
1600
1800
pressure [GPa]
temperature [°C]
Mg0.5Fe2.5Fe2O6
O5 + fper
O4 + fper

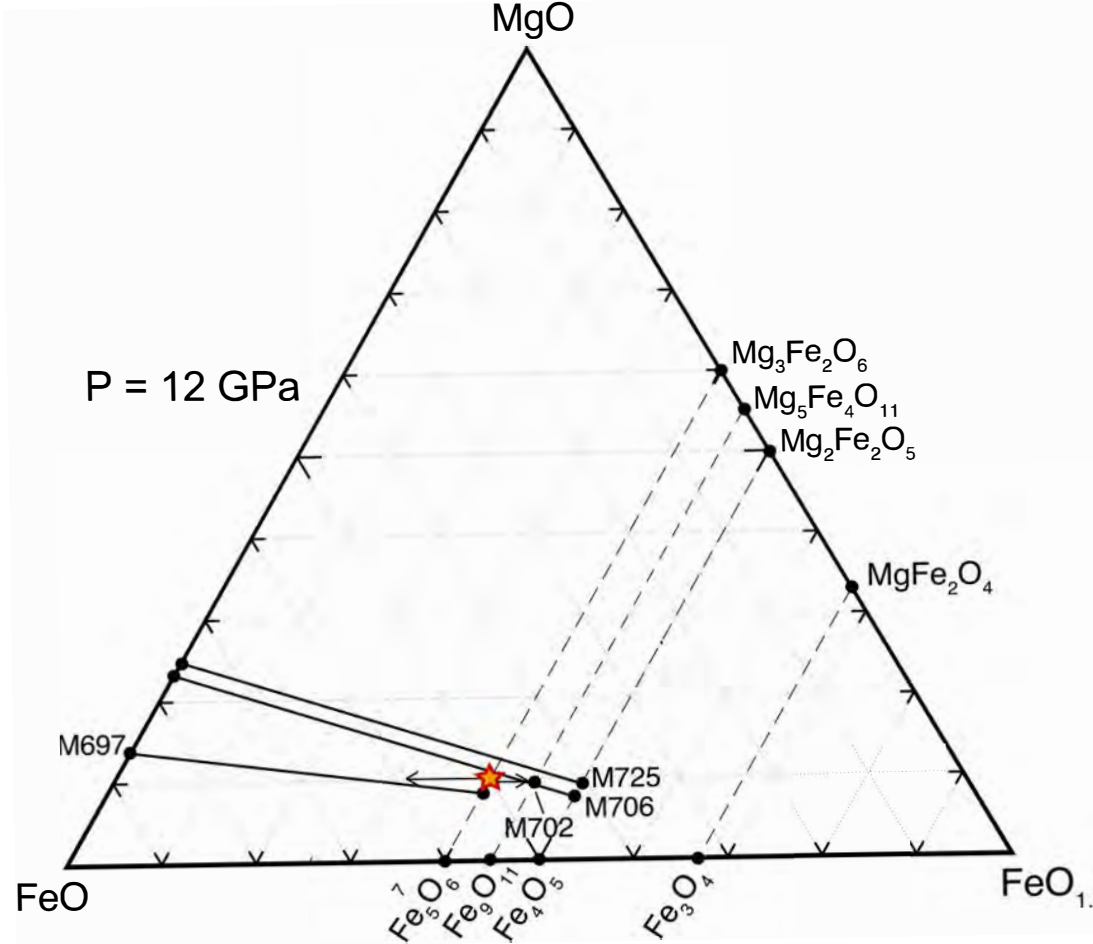
MgO
P = 12 GPa
$Mg_3Fe_2O_6$
$Mg_5Fe_4O_{11}$
$Mg_2Fe_2O_5$
$MgFe_2O_4$
M697
M725
M706
M702
FeO
Fe_5O_6
Fe_9O_{11}
Fe_4O_5
Fe_3O_4
$FeO_{1.}$

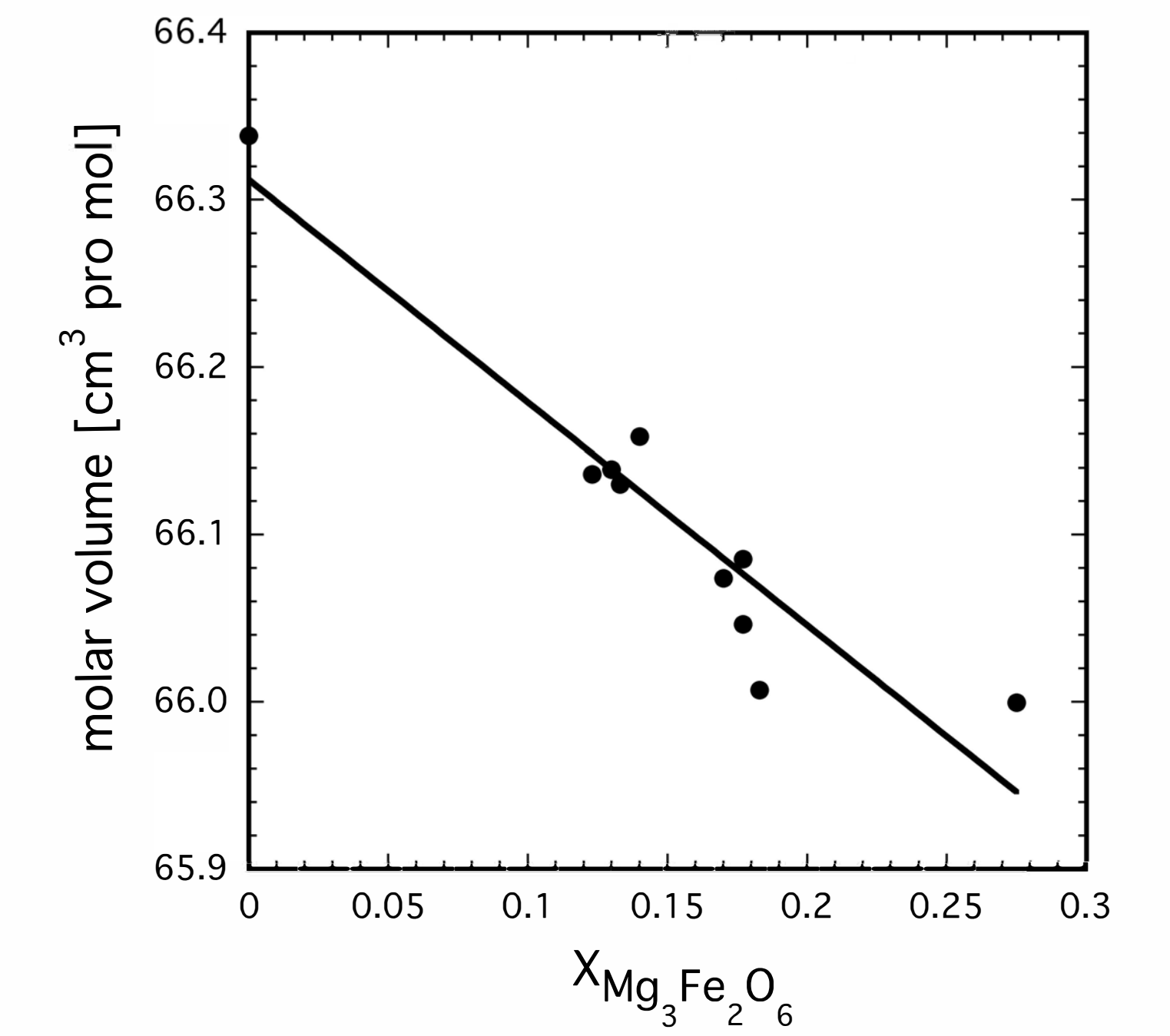
66.4
66.3
66.2
66.1
66.0
65.9
molar volume [cm3 pro mol]
0
0.05
0.1
0.15
0.2
0.25
0.3
XMg3Fe2O6

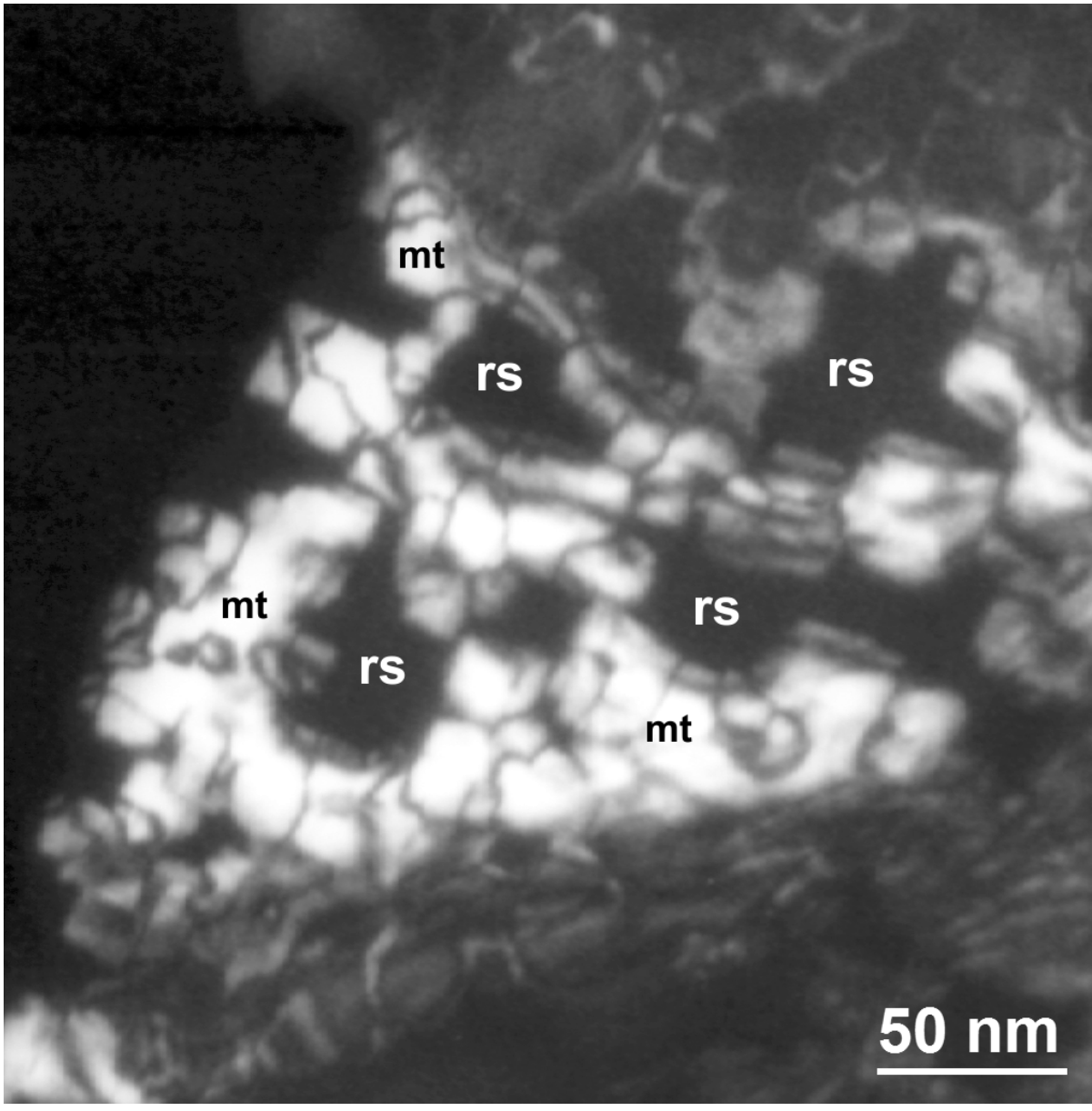

Fig. 11a. Antiphase domains in magnetite from sample M697 that formed by decomposition of the high-pressure Fe_5O_6 phase. rs = rock salt structure (i.e. wüstite), mt = magnetite.

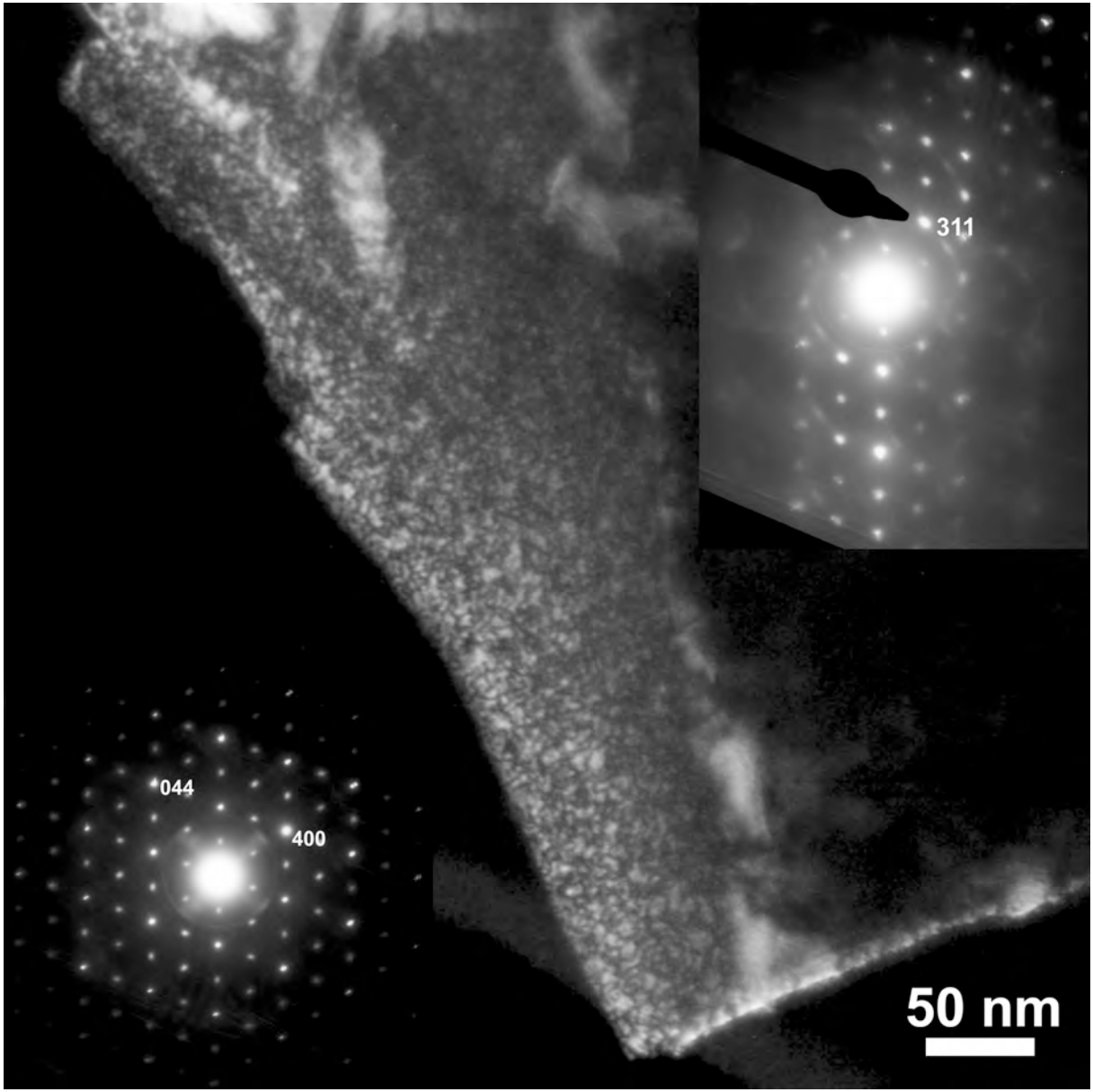

Fig. 11b. Dark-field TEM image with *g* = 311 displaying a mottled contrast in the iron oxide compound that back-transformed from Fe_5O_6 (sample V888). The lower left and upper right insets are SAED patterns of the nearest zone axis and the corresponding diffraction pattern to the DF image, respectively, indicating the presence of magnetite.